Title: *Synaptopodin* KO rat for assessing the dendritic spine apparatus and axonal cisternal organelle in synaptic plasticity, development, and behavior

Running Title: *Synaptopodin* knockout rats

Article Type: Resource

Authors

Masaaki Kuwajima, Olga I. Ostrovskaya, Lyndsey M. Kirk, Ashley Alario, Weiling Yin, Sonia Singh, Anna Xaymongkhol, Adrienne Li, Ella Prasad, Kristen M. Harris

Affiliation

Department of Neuroscience and Center for Learning and Memory, The University of Texas at Austin, Austin, Texas 78712

Corresponding Author and Lead Contact

Masaaki Kuwajima: masa@mail.clm.utexas.edu; Department of Neuroscience, The University of Texas at Austin, 1 University C7000, Austin, TX, 78712

Co-Corresponding Author

Kristen M. Harris: kharris@utexas.edu; Department of Neuroscience, The University of Texas at Austin, 1 University C7000, Austin, TX, 78712

ORCiD

MK: 0000-0002-1478-3726

OIO: 0000-0002-8565-6273

LMK: 0000-0002-5125-652X

AA: 0009-0005-1151-2954

WY: 0009-0006-5574-587X

SS: 0009-0003-6490-8907

KH: 0000-0002-1943-4744

Keywords

neurons, dendritic spines, axon initial segment, synaptic plasticity, endoplasmic reticulum, kidney glomerulus, podocytes, bone development, gene knockout, actin-binding protein

1

Summary

The actin-binding protein synaptopodin (Synpo) regulates the cytoskeleton and intracellular Ca^{2+} and is important for long-term potentiation (LTP) and learning. The inconsistent onset age for LTP in mice makes their *Synpo* knockout (KO) a suboptimal developmental model. Hence, we generated *Synpo* KO rats using CRISPR-Cas9. Synpo KO rats are viable with reduced body weight and bone length after postnatal days (P)35-P45. Their basal kidney function is normal. 3D reconstruction from electron microscopy reveals the absence of the Synpo-dependent dendritic spine apparatus and cisternal organelles in the axon initial segment (AIS), which may contribute to reduced LTP in the KO rat. Inhibitory synapses in the wild-type AIS appear preferentially clustered near cisternal organelles—a pattern disrupted in the KO, where synapses appear more uniformly distributed. The consistent developmental profile of LTP in the rat makes this KO a robust model to assess Synpo function in development, synaptic plasticity, and behavior.

Graphical Abstract
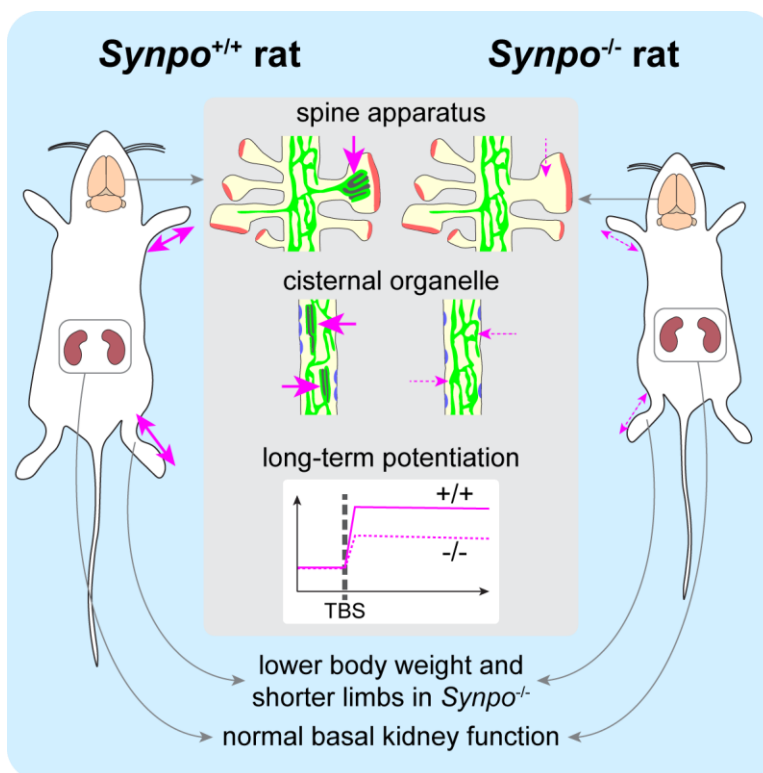
Introduction

Regulation of actin cytoskeleton and intracellular Ca^{2+} is essential for cellular functions, including synaptic plasticity in neurons and glomerular filtration in the kidney. The actin-binding protein synaptopodin (Synpo) is expressed in both neurons and kidney podocytes. Synpo is critically involved in controlling the structure of smooth endoplasmic reticulum (SER)[1–3] that affects Ca^{2+} transients.[4] Synpo regulates actin bundling and stress fiber formation[5] and change in its expression level has been proposed as a biomarker for glomerular diseases, Lewy body dementias, and acute hypoxic brain injury.[6–9]

The short isoform of Synpo is expressed in many forebrain areas, where it is required for the formation of the spine apparatus in dendritic spines and cisternal organelles in axon initial segments. Both structures are derived from multiple cisterns of SER integrated with the actin cytoskeleton and Synpo.[1–3,10,11] The spine apparatus mediates Ca^{2+}-induced Ca^{2+} signaling in dendritic spines[4,12,13] and may contain the molecular machinery for ribosome docking and post-translational modification.[14–17] Synpo is upregulated during long-term potentiation (LTP), a widely studied mechanism of learning and memory.[18,19] Spines containing the spine apparatus undergo greater amounts of plasticity than those lacking this organelle.[20–22] The cisternal organelle also serves as a source of intracellular Ca^{2+} and plays a role in plasticity of the axon initial segment and regulation of neuronal excitability.[2,23–26]

In the foot processes of podocytes in the kidney glomerulus, the long and T isoforms of Synpo promote actin bundling and stress fiber formation mediated by alpha-actinin.[5] This process is regulated by phosphorylation-dependent proteolysis of Synpo.[27–29] Loss of Synpo compromises the foot process function, impairing recovery from nephrotic syndrome induced by the bacterial component lipopolysaccharides[5] or the chemotherapy drug Adriamycin.[30]

A mouse model of *Synpo* deletion has been used to study the role of Synpo in brain and kidney functions. This animal model has revealed that Synpo and the spine apparatus are involved in the induction and maintenance of long-term potentiation and synaptic plasticity.[1,31–35] However, the onset of LTP expression in the mouse hippocampus area CA1 is highly variable over postnatal day (P) 18-37.[36] In contrast, rats have a well-defined onset age for LTP at P12 that coincides with spinogenesis.[37,38] These findings suggest that rats are a more suitable model than mice for establishing the developmental profile of ultrastructural synaptic plasticity.

We previously found that LTP induced by theta-burst stimulation (TBS) in the hippocampal area CA1 of adult rats is associated with the conversion of SER tubules into the spine apparatus, as well as synapse enlargement and clustering around spines containing spine apparatus.[22] In contrast, TBS-induced LTP in juvenile (P15) rats is linked to synaptogenesis rather than SER-associated synapse enlargement.[39,40] Interestingly, Synpo expression is developmentally regulated, with the protein expressed at P5, and reaching adult levels by P12.[41,42] Previous work suggests that the spine apparatus is absent at birth and requires maturation past P15 in rat hippocampus.[43,44] Accordingly, the developmental upregulation of Synpo and formation of the spine apparatus may contribute to the maturation of synapses, spine clustering, and LTP.[22,40]

Here, we generate and investigate *Synpo* knockout (KO) rats. The outcomes demonstrate that KO rats are an important resource for probing the impact of *Synpo* deletion on brain, bone, and kidney functions, especially during development, learning, memory, and a variety of disease processes.

4

Results

We used the CRISPR-Cas9 system to delete the coding region of the *Synpo* gene in rats (Figs. 1A, B), designing guide RNAs to target the 5' and 3' regions flanking the protein-coding exons 2 and 3. The successful deletion was confirmed by sequencing the PCR products spanning the excised region from N1 generation rats (Document S1). The resulting two KO lines carry alleles that differ in the genomic location of the 5' breakpoint
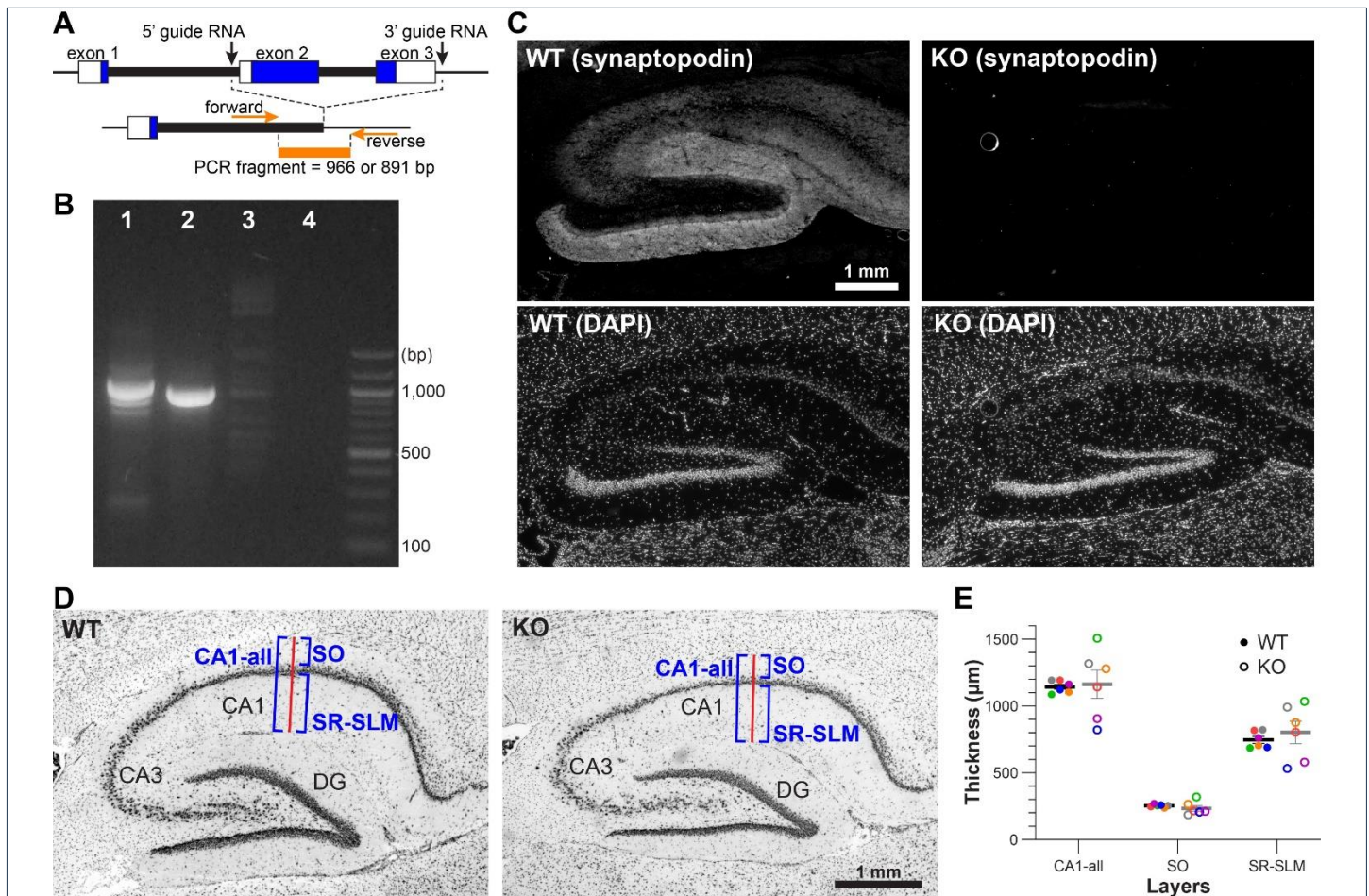

Figure 1. Generation of congenital *Synpo* KO rat.
(A) Schematic of the rat *Synpo* gene structure. *Top:* WT gene structure with guide RNA targeting sites (black arrows) flanking exons 2 and 3. *Bottom:* KO gene structure with locations of forward and reverse PCR primers used to confirm deletion (orange arrows). Blue box = protein-coding exons; white box = untranslated exon regions; thick lines = introns; thin lines = flanking genomic DNA; orange line = expected PCR fragment with successful deletion. (Also see Document S1.) (B) PCR products from two founder lines show fragments with expected sizes (Lane 1 = Allele A, 966 bp; Lane 2 = Allele B, 891 bp). Lane 3 = WT; PCR band is absent because the conditions do not support amplification of the longer wild-type sequence. Lane 4 = no DNA negative control.
(C) Synpo protein is absent in the KO hippocampus.
(D) Representative brightfield micrographs of the WT (left) and KO (right) hippocampus in parasagittal sections stained with Cresyl Violet. In the area CA1, the thickness of layers (CA1-all, SO, and SR-SLM, delineated by blue brackets) was measured along the red line that originates at the dorsal-most point of the hippocampus and crosses *stratum pyramidale* perpendicularly, ending at the hippocampal fissure.
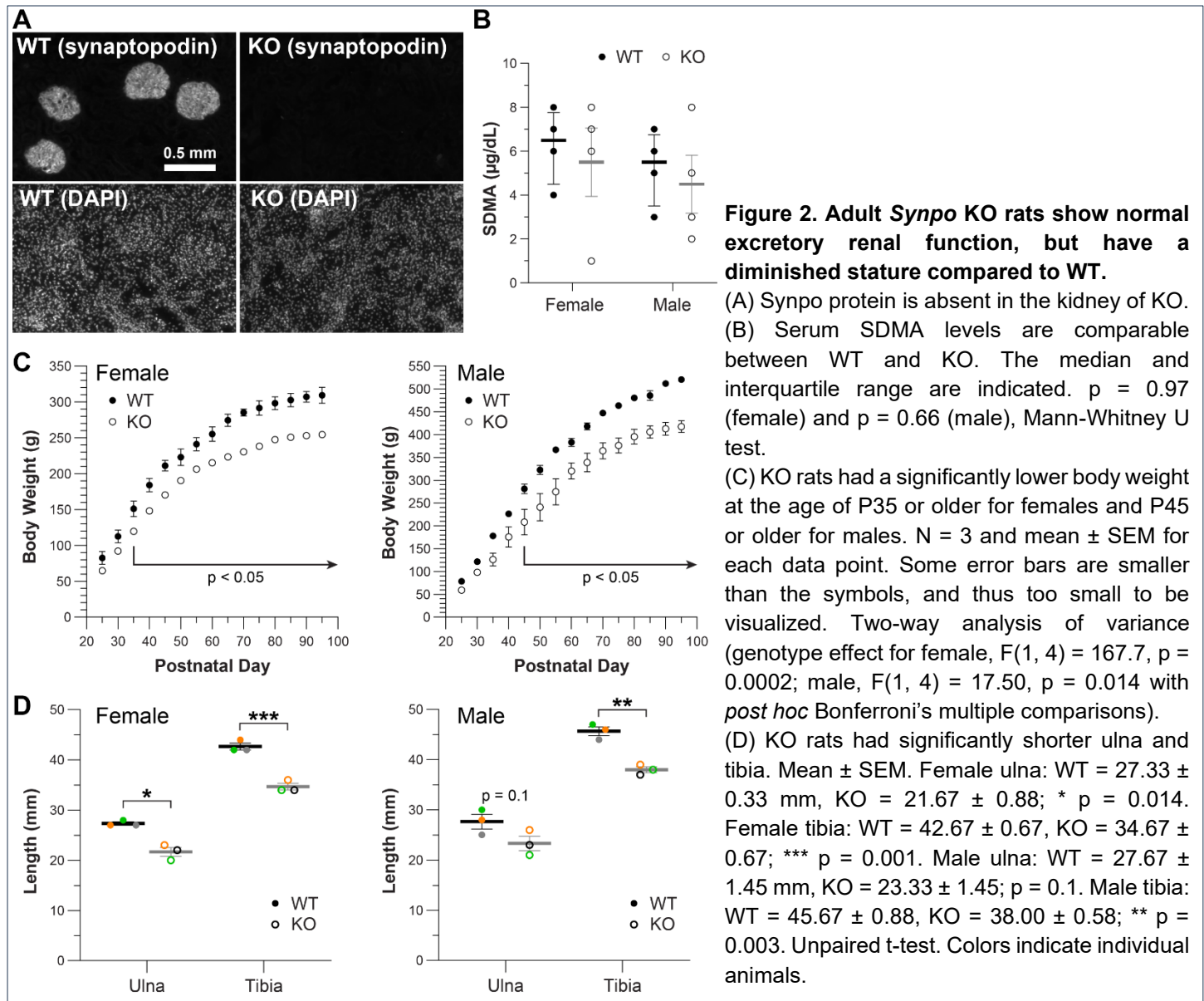(E) Quantification shows that CA1 layer thickness was not altered in KO (mean ± SEM; unpaired t-test; n = 6 sections from 3 animals per genotype; colors indicate individual animals). CA1-all: WT = 1142.69 ± 18.62 μm, KO = 1161.73 ± 106.13; p = 0.87. SO: WT = 253.60 ± 4.52, KO = 233.67 ± 20.21; p = 0.22. SLM: WT = 746.10 ± 25.38, KO = 802.88 ± 85.14; p = 0.54.

(Document S1). The KO rats are viable and appear healthy into adulthood under standard laboratory housing conditions. When heterozygotes were paired for breeding, the resulting litter size averaged 11, ranging from 4 to 18 pups (based on 51 litters from 20 breeding pairs). Both KO lines were used to measure body weight (Fig. 2C) and were prepared for electron microscopy to ensure deletion of the spine apparatus (Fig. 3) and cisternal organelle (Fig. 4). After the first line was deposited to the Rat Resource and Research Center (Columbia, MO; https://www.rrrc.us), under the designation LE-Synpo[em1Kmh], the second line (LE-Synpo[em2Kmh]) was used for histology (Figs. 1D and E), renal function tests (Fig. 2A), bone length measurements (Fig. 2D), and slice physiology (Fig. 5).

The absence of Synpo protein in the KO was confirmed with immunohistochemistry labeling of the hippocampus (Fig. 1C), where Synpo is highly expressed in WT rats. Gross hippocampal morphology was indistinguishable between WT and KO rats. Specifically, there was no statistically significant difference in the thickness of the CA1 layers, including the *stratum oriens* (SO), the combined *strata radiatum* and *lacunosum-moleculare* (SR-SLM), or the entire CA1-all region (Figs. 1D and E). Thus, the overall laminar organization of this hippocampal region remains normal in KO rats, a finding consistent with studies in KO mice.[1]

Synpo is also expressed in the kidney glomerulus,[5,41] where its long and T isoforms modulate Rho signaling and actin bundling in podocytes.[27,29] Although their basal urinary protein excretion was reported to be normal,[1] *Synpo* KO mice exhibited a delayed recovery from proteinuria during a model of transient nephrotic syndrome.[5,30] The kidney-specific Synpo isoforms are encoded by exons 2 and 3 that were deleted in our rat lines, with their absence in the KO kidney confirmed by immunofluorescence labeling (Fig. 2A). We also assessed the levels of symmetric dimethylarginine (SDMA) in blood serum samples collected from WT and KO. SDMA is a byproduct of intranuclear arginine methylation and serves as a biomarker correlating with glomerular filtration rate in multiple mammalian species, including the rat.[45–48] No statistically significant difference was detected in the serum SDMA levels between WT and KO rats (Fig. 2B), suggesting that the basal kidney function remains normal in the absence of Synpo. However, over a period of 288 days, 3 KO rats (2 males and 1 female) out of 20 total developed acute renal failure and were euthanized at ages between P105 and P157. During the same period, acute renal failure was not seen in any of the 26 WT or 28 heterozygous littermates P100 or older, or 38 WT and 43 KO that were at P99 or younger. These findings suggest that some KO rats may be more susceptible to conditions of kidney stress later in adulthood.

Unexpectedly, the KO rats appeared smaller in stature than the WT littermates. We tracked their body weight between P21 and P100. For both females and males, KO rats weighed significantly less from P35 onward for females and from P45 onward for males (Fig. 2C). We also found that the length of the tibia and ulna in young adult female KO rats (P58-72) were significantly shorter than wild-type littermates, and the tibia was significantly shorter in KO male rats of the same ages (Fig. 2D). Thus, body size differences between genotypes become significant after the first several weeks of postnatal development, a factor that may affect interpretation of behavioral tests that depend on locomotion as a measure of performance.

Figure 2. Adult *Synpo* KO rats show normal excretory renal function, but have a diminished stature compared to WT.

(A) Synpo protein is absent in the kidney of KO.
(B) Serum SDMA levels are comparable between WT and KO. The median and interquartile range are indicated. $p = 0.97$ (female) and $p = 0.66$ (male), Mann-Whitney U test.
(C) KO rats had a significantly lower body weight at the age of P35 or older for females and P45 or older for males. N = 3 and mean ± SEM for each data point. Some error bars are smaller than the symbols, and thus too small to be visualized. Two-way analysis of variance (genotype effect for female, $F(1, 4) = 167.7$, $p = 0.0002$; male, $F(1, 4) = 17.50$, $p = 0.014$ with *post hoc* Bonferroni's multiple comparisons).
(D) KO rats had significantly shorter ulna and tibia. Mean ± SEM. Female ulna: WT = 27.33 ± 0.33 mm, KO = 21.67 ± 0.88; * $p = 0.014$. Female tibia: WT = 42.67 ± 0.67, KO = 34.67 ± 0.67; *** $p = 0.001$. Male ulna: WT = 27.67 ± 1.45 mm, KO = 23.33 ± 1.45; $p = 0.1$. Male tibia: WT = 45.67 ± 0.88, KO = 38.00 ± 0.58; ** $p = 0.003$. Unpaired t-test. Colors indicate individual animals.

The spine apparatus and other SER-derived structures were quantified using three-dimensional reconstruction from serial section electron microscopy (3DEM) of axo-spinous synapses in CA1 *s. radiatum* of the WT and KO rat (Fig. 3). The spine apparatus was identified as consisting of two or more cisterns of SER

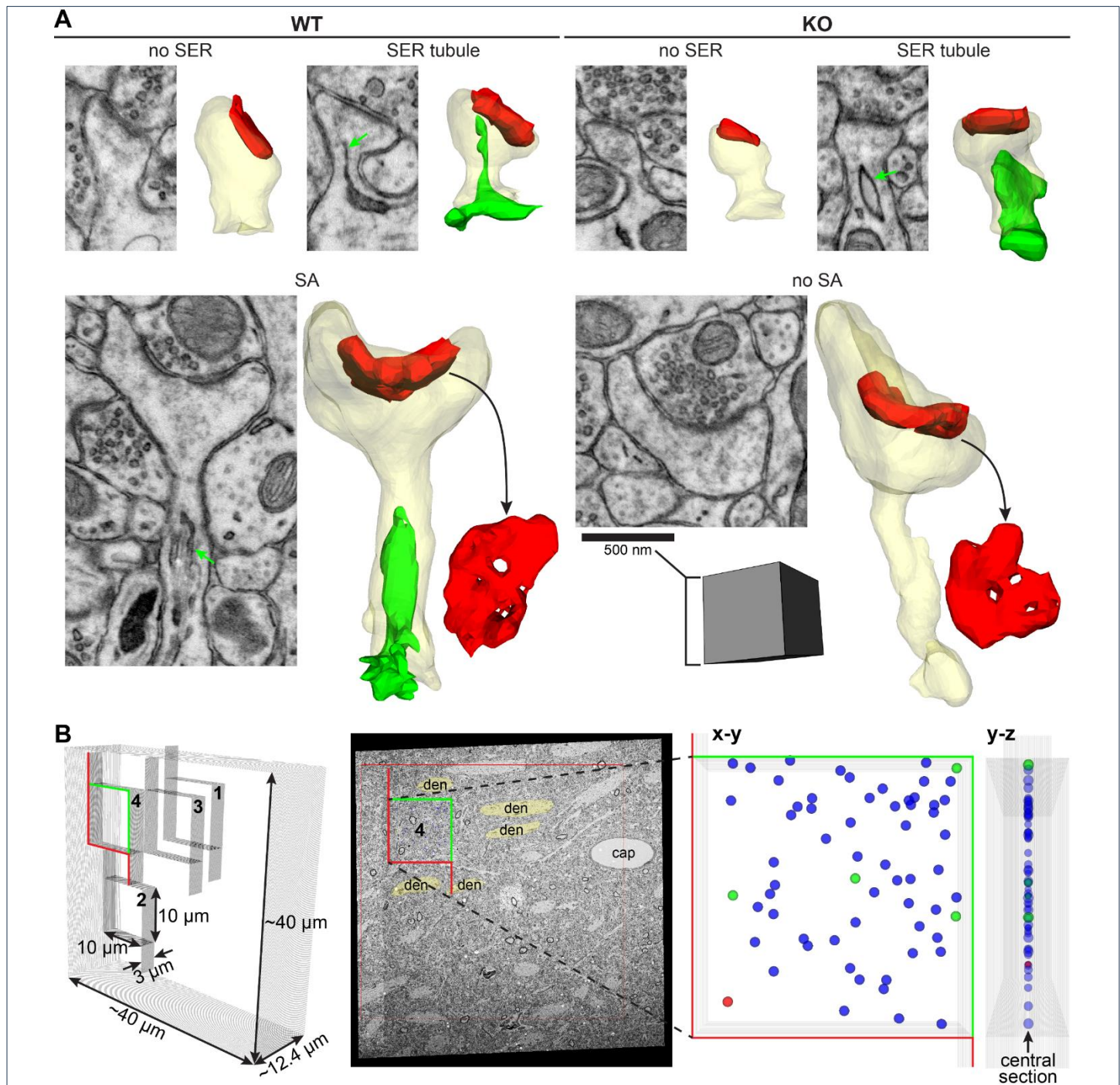with interdigitating dense plates, while an SER tubule in a spine is a membrane-bound structure that is

Figure 3. The spine apparatus is absent in *Synpo* KO rat.
(A) EM images and 3D reconstructions of dendritic spines (transparent yellow) and their PSDs (red) in WT and KO, with no SER, SER tubule, or SA (green). KO rats had spines and PSDs as large as those in WT, but no SA were observed. (B) Sample regions of interest (ROI), this example from WT. *Left* – A schematic view of four ROIs (labeled 1-4; 10 μm × 10 μm × 3 μm each) placed within nonoverlapping locations in one of four EM series (n = 2 per genotype) each encompassing ~40 μm × ~40 μm × ~12 μm. *Middle* – Each ROI (a sampling frame for ROI #4 is shown) was placed on the central section avoiding large structures such as apical trunk dendrites (den) and capillaries (cap). *Right* – A schematic view of the ROI #4 in x-y and y-z planes, with colored spheres representing all PSDs that occurred on the central section within the sampling frame. PSDs that cross the green inclusion lines are included, while those crossing the red exclusion lines are excluded from analysis. The identified PSDs were categorized according to the presence of the spine apparatus (red sphere), smooth endoplasmic reticulum (green spheres), or absence of SER or spine apparatus (blue spheres) in the spines. Quantification is summarized in Table 1.

contiguous with the SER network in the parent dendritic shaft (Fig. 3A). We adapted the unbiased 3D brick method[49] to determine the relative frequencies of SER tubules and the spine apparatus (Fig. 3B). For each of four EM series from *s. radiatum* (2 WT and 2 KO), four non-overlapping sub-volumes (300 µm^3 each) were selected in the neuropil, avoiding large structures such as cell bodies, capillaries, apical trunk dendrites, myelinated axons, and proximal processes of astrocytes. All postsynaptic densities of axo-spinous synapses that appeared in the middle section of each sub-volume were identified. Then the associated spines were followed to determine the absence or presence of an SER tubule or spine apparatus in the spines (Fig. 3B). The density of axo-spinous PSDs was comparable between WT and KO, suggesting that *Synpo* deletion does not disrupt the number of synapses. Most spines in both conditions lack an SER tubule or spine apparatus (Fig. 3, Table 1). A single SER tubule occurs in about 6% of WT spines and 4% of KO spines (Fig. 3, Table 1). A spine apparatus occurred in 5% of the WT, but none occurred in the KO (Table 1), even when compared qualitatively to spines of similar sizes (Fig. 3A).

Using 3DEM, we also sampled the axon initial segments (AIS) located at the border between CA1 *strata pyramidale* and *oriens.* AISs were identified by visual inspection through serial sections for the presence of fasciculated microtubules and dense undercoating along the intracellular face of the plasma membrane.[50,51] Like the spine apparatus, the cisternal organelles form a complex made of at least two SER cisterns with interdigitating dense plates (Fig. 4A, EM). A total of 118 cisternal organelles were observed in the 18 AIS with lengths of 7-39 µm in the 2 WT series (Table 2). No cisternal organelles were found in the 15 AISs with lengths of 9-61 µm from 2 KO series (Table 2). One AIS each from a WT (Fig. 4A) and a KO (Fig. 4B) was fully reconstructed, including all synapses, cisternal organelles, and SER. The SER cisterns of the WT organelles

Table 1. Quantification of asymmetric axo-spinous synapses and the presence of SER-derived structures in their spines.

	N	ROI Area (µm^2)	PSDs Total Number	PSDs /µm^2	no SER	SER tubule	SA
WT	2, 2, 8	100	473	0.59 ± 0.031	419 (89%)	29 (6%)	25 (5%)
KO	2, 2, 8	100	516	0.65 ± 0.029	495 (96%)	21 (4%)	0 (0%)

(N = number of animals, series, ROIs. PSD density did not differ between WT and KO, mean ± SEM, n = 8 ROIs per genotype, p = 0.22, unpaired t-test.)
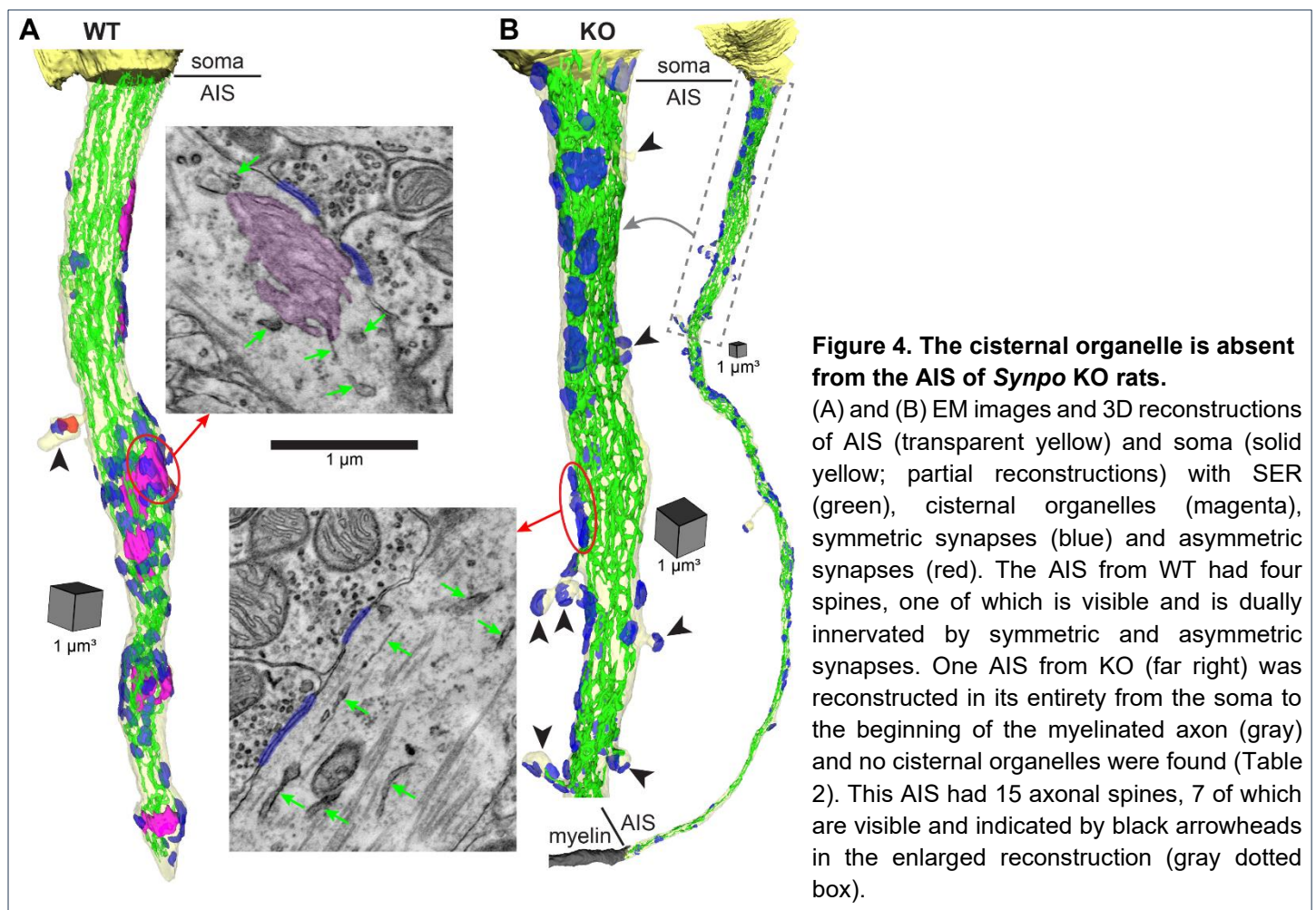
Table 2. Quantification of AIS and cisternal organelles.

	N	Serial Sections (n)	Sample volume (µm^3)	AIS (n)	AIS lengths (range; µm)	Cisternal Organelles (total count)
WT	2, 2	297, 225	33,728, 26,578	17	7.2 - 38.5	118
KO	2, 2	302, 182	37,944, 21,988	15	9.7 - 61.4	0

(N = number of animals, number of series.)

were continuous with the SER network spanning the entire length of the AIS. In contrast, the AIS from KO

contained no cisternal organelles despite having a robust SER network (Fig. 4B).

Putative inhibitory synapses are identified by symmetrically thin presynaptic and postsynaptic

thickenings and smaller pleomorphic presynaptic vesicles compared to putative excitatory synapses on

dendritic spines (compare EM images of synapses in Fig. 4 with Fig. 3A). Reconstruction of an AIS from the

WT suggests that the symmetric synapses are clustered along the AIS around the cisternal organelles (Fig.

4A). In contrast, synapses in the KO appear to be more evenly distributed along the length of the AIS (Fig. 4B).

This reconstructed KO AIS had a total of 15 axonal spines, with 11 having at least one inhibitory synapse, and

the remaining four being nonsynaptic protrusions. Interestingly, one of the four AIS axonal spines in the WT

reconstruction is dually innervated by an excitatory and an inhibitory synapse (Fig. 4A). Visual inspection of the

other AIS with axonal spines in WT (21 from 8 AIS) and KO (15 from 4 AIS) revealed they were innervated by

1-4 synapses in both genotypes.

Figure 4. The cisternal organelle is absent from the AIS of *Synpo* KO rats.
(A) and (B) EM images and 3D reconstructions of AIS (transparent yellow) and soma (solid yellow; partial reconstructions) with SER (green), cisternal organelles (magenta), symmetric synapses (blue) and asymmetric synapses (red). The AIS from WT had four spines, one of which is visible and is dually innervated by symmetric and asymmetric synapses. One AIS from KO (far right) was reconstructed in its entirety from the soma to the beginning of the myelinated axon (gray) and no cisternal organelles were found (Table 2). This AIS had 15 axonal spines, 7 of which are visible and indicated by black arrowheads in the enlarged reconstruction (gray dotted box).

Next, we analyzed the impact of *Synpo* deletion on LTP in the rat hippocampal area CA1. Field excitatory postsynaptic potentials (fEPSPs) were recorded in *s. radiatum* of acute hippocampal slices from WT and KO. The stimulus/response curves did not differ significantly between the WT and KO, suggesting basal synaptic transmission was not affected by the *Synpo* deletion (Fig. 5A). Stimulus intensities set to ~50% of maximal yielded comparable baseline fEPSPs across experiments and genotypes (WT = 0.95 ± 0.4 mV/ms; KO = 1.09 ± 0.5; mean ± SD). A moderate LTP induction protocol, consisting of 3 trains of theta-burst stimulation (TBS, 3T), revealed impaired LTP in slices from KO rats compared to WTs when measured 1 hr after TBS (Fig. 5B). However, by 2 hr after 3T the difference in LTP magnitude between WT and KO was no
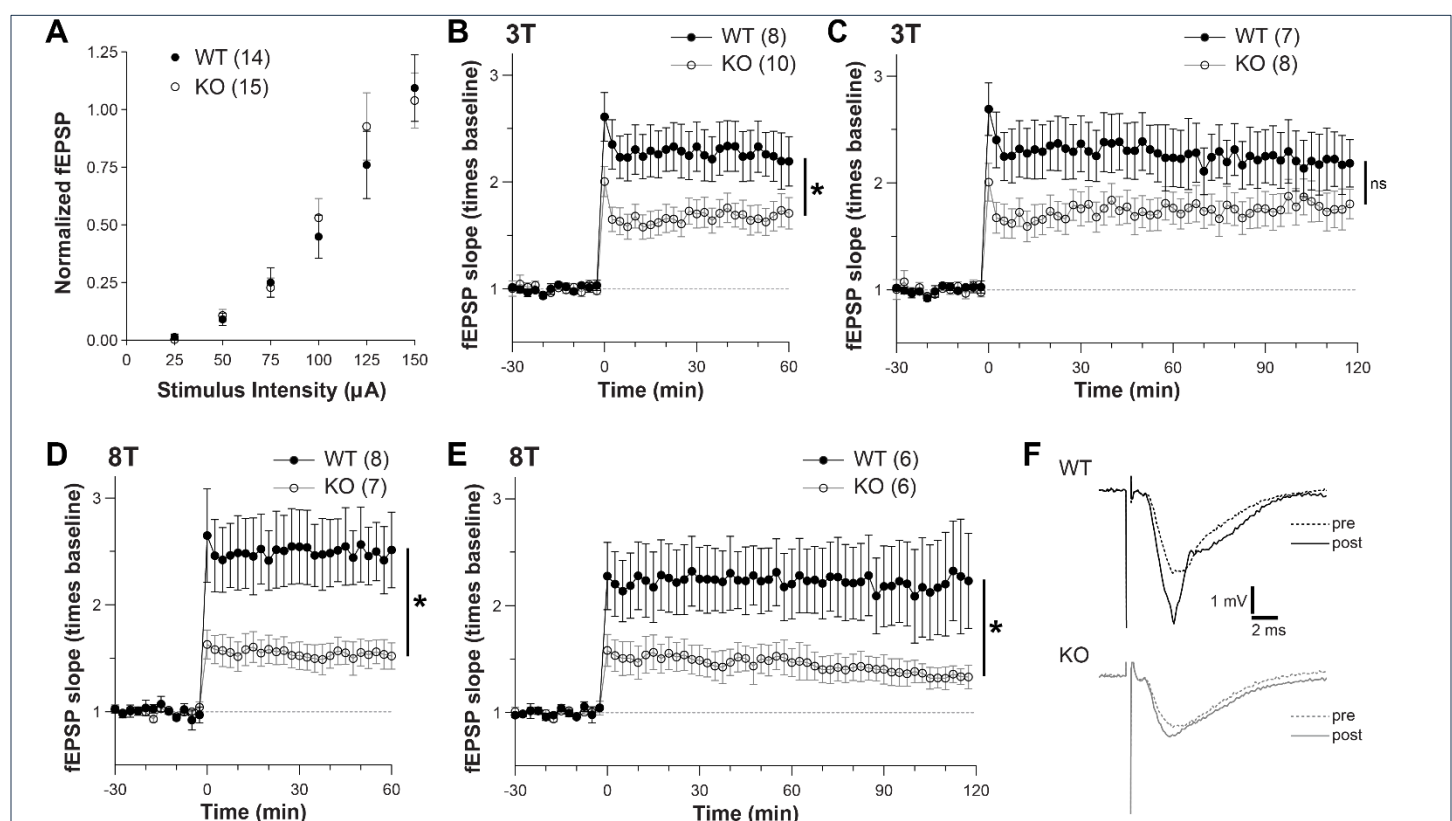
Figure 5. Early LTP is consistently impaired in the *Synpo* KO rats while later LTP is dependent on the induction paradigm.

(A) Overlapping stimulus-response curves for WT and KO. Data were collected prior to baseline recordings during experiments using 3 trains (3T) or 8 trains (8T) of TBS.

(B) LTP induced by 3T at time 0 is impaired in *Synpo* KO at 1 hr after TBS. (WT = 2.29 ± 0.23; KO = 1.68 ± 0.13; *p < 0.05, Mann-Whitney U test.)

(C) The difference between WT and KO at 2 hr after 3T is not statistically significant (ns).

(D) and (E) LTP induced by 8T at time 0 is impaired in Synpo KO at both (D) 1 hour and (E) 2 hours after delivery of 8T. (At 1 hr: WT = 2.54 ± 0.35 and KO = 1.55 ± 0.13. At 2hr: WT = 2.18 ± 0.52 and KO = 1.35 ± 0.1; *p < 0.05, Mann-Whitney U test.)

(F) Waveforms from the 8T experiments show example pre- and post-8T responses at 2 hr.

(Numbers in parentheses above each graph in A-E indicate the number of slices in each experiment. In total, 7 WT and 8 KO rats were used.)

11

longer statistically significant (Fig. 5C). In contrast, a stronger, saturating LTP protocol with 8 trains of TBS produced less LTP at both times in the KO (Fig. 5D-F).

Discussion

We report generation of two rat lines with congenital deletion of both exons 2 and 3 of *Synpo* using a CRISPR-Cas9 approach. Although viable, KO rats exhibit reduced body size and shortened limbs. Despite normal hippocampal histology, they lack both the spine apparatus and cisternal organelle and display impaired long-term potentiation (LTP). As in KO mice, a subset of KO rats is susceptible to kidney stress in adulthood. While some differences between the rat and mouse Synpo KO are subtle, others are profound, especially in relation to Synaptopodin function in development and synaptic plasticity.

The basal excretory renal function in our rat KO is normal based on the SDMA data. In previous studies, dipstick proteinuria was not significantly different between KO and WT mice.[5] One mouse KO model had only exon 2 deleted, and expression of Synpo-T (an isoform encoded by exon 3) was elevated in the kidney of the KO.[5] When these KO mice were challenged with lipopolysaccharides, a model of transient nephrotic syndrome, they recovered, but more slowly than their WT counterparts. The delayed recovery was attributed to a slower re-formation of podocyte actin filaments partially supported by Synpo-T. Another KO mouse model lacking all three Synpo isoforms did not develop kidney abnormalities up to 12 months of age, but they were more susceptible to nephropathy induced by Adriamycin.[30] Since both exons 2 and 3 of the *Synpo* gene are deleted in the KO rat, all three Synpo isoforms are absent, which might contribute to the acute renal failure observed in only 3 KO that were P105 or older. These results suggest that KO rats can be studied during development and in young adulthood without concern for kidney malfunction.

KO rats older than P35 (females) or P45 (males) are smaller in stature than their WT littermates, as measured by body weight and limb bone length. It is not known whether the smaller stature of the KO might be secondary to subclinical levels of kidney dysfunction, which indirectly affects calcium reabsorption,[52,53] or to a direct role for *Synpo* in musculoskeletal development. An RNA-seq study of 11 organs in Fisher rats showed that heart, muscle, and lungs express *Synpo* transcripts at least as much as the brain and kidney, but bone tissue was not included.[54] Previous reports from KO mice indicate their appearance was indistinguishable from

12

WT although weights and bone dimensions were not reported.[1] The small size of mice makes it harder to detect and measure subtle but important differences in bone length and body mass. Mice also express *Synpo* transcript in the heart, lungs, and limbs.[55] Thus, the potential involvement of *Synpo* in limb maturation could confound behavioral analyses, such as the reduced horizontal locomotor activity observed for KO mice in the open-field test.[1] Being able to assess when during development the gross body effects occur in the KO is thus an advantage for the rat KO model system.

SER is a continuous internal membrane that extends from the cell body into axons, dendrites, and some spines.[43,56–59] SER regulates calcium dynamics and homeostasis, and the synthesis and trafficking of lipids and proteins.[60,61] SER is a limited resource that makes brief visits to active spines,[62] which may explain why SER occurs in less than 15% of hippocampal CA1 spines at any one time.[22,43,44] We found a comparable proportion of dendritic spines contains an SER tubule in both KO and WT rats, suggesting the capacity for SER to visit spines is not lost in the Synpo KO.

The spine apparatus is a specialized structure derived from SER and dense plates of Synpo.[3,63] In addition to its SER-related functions, the spine apparatus is often associated with ribosomes and polyribosomes, indicating a role in local protein synthesis.[14,16] Secretory pathway proteins found in the Golgi apparatus are also present in the spine apparatus, suggesting involvement in local post-translational modifications critical for maturation and correct trafficking of proteins.[15] The largest synapses occur on dendritic spines that contain SER, especially in the form of the spine apparatus. By 2 hours after the induction of LTP, the predominant type of SER contained in spines shifts from a single tubule under control conditions to a fully elaborated spine apparatus.[22] LTP induces dramatic PSD enlargement in spines with SER, while spines without SER undergo a comparatively smaller increase in PSD size. In addition, dendritic spines tend to cluster in the vicinity of large spines that contain SER. Intracellular trafficking slows where the dendritic shaft SER branches or expands, allowing ER exit sites to locally deliver resources that support clustered synapses.[64] High density spine clusters are longer and have more SER branches than low density clusters. Following LTP, the density of spines in a cluster that has an SER-containing spine remains high and total synapse area is elevated as these synapses enlarge. In contrast, spine density in a cluster without SER-containing spines remains low or is further reduced following LTP. Furthermore, high-density clusters display fewer SER branches in the dendritic shaft post-LTP, possibly reflecting migration of SER into spines to support PSD growth and elaboration of the spine apparatus.[22] The spine apparatus is

eliminated in the *Synpo* KO, yet qualitative observations suggest that spines of comparable sizes could be found in the KO and WT of our rat and in the mouse.[1] Future work will be needed to determine whether spines and synapses reach maximal size in the KO and whether clustering of small spines around enlarged spines can be enhanced during plasticity.

Axo-axonic GABAergic interneurons, also known as Chandelier cells, selectively target the AIS of excitatory pyramidal neurons in hippocampal area CA1 and other excitatory pyramidal neurons throughout the brain. This network is important in many normal brain functions such as slow wave sleep and circuit excitability.[65] Dysfunction of the axo-axonic network has been linked to schizophrenia, epilepsy, and autism spectrum disorder.[66] Synpo is required for the formation of cisternal organelles in the AIS of mice.[2] Hence, the absence of the cisternal organelles in the AIS of the CA1 pyramidal cells in our KO rat is expected. Reconstruction of the CA1 AIS from a WT rat suggests inhibitory synapses cluster around the cisternal organelles, as was previously reported for neocortical pyramidal neurons.[67] In our KO rats, the clustering of inhibitory inputs on the AIS appears to be lost, although inhibitory synapses are still present and more uniformly distributed along the AIS. Although LTP in CA1 is usually associated with glutamatergic synapses and plasticity in other interneuron types (including those targeting dendrites or soma), the spatial arrangement of axo-axonic synapses at the axon initial segment could indirectly influence plasticity by modulating pyramidal neuron firing patterns.[68]

Multiple factors could contribute to the differential impact of *Synpo* deletion on LTP in KO mice versus KO rats. In mice, the greater neuronal density compared to rats can affect synaptic connectivity, network activity, neuronal excitability, as well as the expression of synaptic plasticity.[69–72] We evaluated LTP induction and maintenance using 3T and 8T TBS protocols consistent with one of the original KO mouse studies and our previous rat studies.[1,39,73] Both protocols result in reduced LTP in the *Synpo* KO rat at 1 hr after induction. LTP remains impaired at 2 hr after induction by 8T but not by 3T in the KO rats, contrasting with the KO mice that remained impaired at 2 hr after 3T.[1] LTP induction protocols varied greatly across KO mouse studies including tetanic stimulation at 100 Hz[1,33,35] versus TBS for 1T, 3T, or 5T.[1,32] These distinct stimulation patterns could activate different molecular pathways[74] and recruit varying numbers of presynaptic axons. Age also plays an important role in LTP ranging from P15 to 6 months for the various studies of LTP in KO mice. Zhang et al. showed, for example, that LTP was impaired in juvenile but not adult KO mice.[32] The dramatic difference

14

between the normal developmental onset and maturation of LTP across ages P18-P37 in mice[36] contrasts with the discrete onset age at P12 in the rat,[38] which likely contributes to the differential effects between mice and rats of *Synpo* KO on the expression of LTP.

The spine apparatus plays a critical role in health and disease, as demonstrated by its aberrant morphology in neurodegenerative and peritumoral brain tissue. Downregulation of Synpo has also been linked to Alzheimer's disease, inflammation, stress, and embryonic hypoxia.[8,75–79] Emerging evidence also supports the use of Synaptopodin as a biomarker for other neural diseases, including frontotemporal dementia, multiple sclerosis, and acute brain injury.[9,80,81]

The effect of *Synpo* deletion on bone development and body growth could be mitigated by a tissue- and time-specific deletion strategy, using, for example, the Cre-lox recombination system.[82,83] Such an approach would allow the animals to develop normally into adulthood before the gene of interest is excised in an inducible manner. However, an inducible KO model is not practical to assess the role of Synpo during development because the Synpo protein has a half-life of about 10 days and is expressed soon after birth by P5, which is well before the spine apparatus forms.[42,43,84] Our congenital KO rat is thus a valuable resource for investigating the function of Synpo during the first 40 postnatal days of life when animals show little or no confounding kidney, bone, or weight gain defects.

15

Materials and Methods

This study was carried out in accordance with the US National Research Council's Guide for the Care and Use of Laboratory Animals, the US Public Health Service's Policy on Humane Care and Use of Laboratory Animals, and the Guide for the Care and Use of Laboratory Animals. All animal procedures were approved by the Institutional Animal Care and Use Committee at The University of Texas at Austin. All rats were housed under 12-hr light/dark cycles with water and food available *ad libitum* in an AAALAC-accredited facility managed by the UT-Austin Animal Resource Center. All efforts were made to minimize suffering.

Congenital *synaptopodin* knockout lines

The *Synpo* KO lines were generated at Mouse Genetic Engineering Facility at UT-Austin (RRID:SCR_021927) using an approach based on the CRISPR-Cas9 system. Synthetic guide RNAs were designed to target 5' and 3' regions flanking the protein-coding regions of the *Synpo* gene, exons 2 and 3, using CRISPOR (version 4.7; https://crispor.org; RRID:SCR_015935) (Fig. 1A and Document S1).[85] The efficacy of these guide RNAs was tested in cultured rat embryos, and the best ones were then used *in vivo*. Injection of the 5' and 3' guide RNAs together into rat embryos resulted in two founder lines with congenital *Synpo* deletion (Fig. 1B, lanes 1 and 2). These lines were bred and maintained separately because their alleles differ in the genomic location of the breakpoints (see Document S1). Genotypes of the animals were confirmed before weaning (postnatal day 10-17) and again at the time of euthanasia for experiments (genotyping performed by Transnetyx, Cordova, TN). The lines were generated and maintained in the Long-Evans background (Charles River strain 006; Crl:LE; RRID:RGD_2308852), and a new WT rat was introduced about every 5 generations to prevent genetic drift. The KO lines are designated as LE-Synpo[em1Kmh] (RRID:RRRC_00964) and LE-Synpo[em2Kmh] (RRID:RRRC_01025) and have been registered with the Rat Genome Database (https://rgd.mcw.edu) as RGD ID 155782907 and RGD ID 616335891, respectively.

Vaginal smear cytology

All adult female rats were used during diestrus when circulating estradiol is low and relatively stable. The vaginal smear cytology was measured on the day of the experiment and several days prior. The estrous cycle of each rat was monitored by performing daily vaginal lavage using 20 µl sterile saline and recording cell

16

morphology on glass slides under an upright microscope at x10 magnification. Diestrus is characterized by the highest proportion of leukocytes.[86–88]

Brain and kidney tissue for light microscopy

For immunofluorescence labeling and histology staining, the rats (n = 3 per genotype; P80) were rapidly decapitated under heavy isoflurane anesthesia. The brain was removed from the cranium, rinsed with phosphate-buffered saline (PBS), and bisected along the midline. Both hemispheres were placed on a metal spatula with the cut surface down and frozen in 2-methyl butane cooled with dry ice. The kidney was also dissected out and frozen as a whole in the same manner. The frozen tissue was stored at -80°C until being cut into sections at 20 μm thickness using a cryostat. The brain sections were cut in the parasagittal plane. The sections were mounted on glass microscope slides and were stored at -80°C until they were used for immunolabeling or histology staining.

Immunofluorescence labeling

The slide-mounted sections were thawed and fixed in 4% formaldehyde in 0.1 M phosphate buffer (PB; pH = 7.4) for 20 min at RT. After PBS washes, the sections were incubated with blocking solution (Animal-Free Blocker® and Diluent; Vector Laboratories, Newark, CA; catalog# SP-5035) containing 0.3% Triton X-100 for 1 hr. The sections were then incubated with rabbit anti-synaptopodin (1:500; Synaptic Systems, Göttingen, Germany; catalog# 163002; RRID:AB_887825) in PBS with the Vector blocking reagent and 0.3% Triton X-100 for overnight at RT. Following PBS washes, the sections were incubated with goat anti-rabbit IgG conjugated with Alexa Fluor 488 (1:100; Thermo Fisher Scientific, Waltham, MA; catalog# A-11034; RRID:AB_2576217) in the same diluent for 1 hr at RT. The sections were washed with PBS and stained with 4′,6-diamidino-2-phenylindole (DAPI) for 5 min. Following washes with PBS and saline (0.9% NaCl, aq), coverslips were applied with Aqua-Poly/Mount anti-fade mountant (Polysciences, Warrington, PA; catalog# 18606). In control experiments, the primary antibody was omitted to confirm the lack of non-specific binding of the secondary antibody, and both the primary and secondary antibodies were omitted to assess background autofluorescence. The primary antibody was raised against a recombinant peptide corresponding to amino acids 331–452 of the mouse Synpo that is conserved in the rat. This antibody recognizes all isoforms of

17

Synpo, and its specificity has been validated by Western blot with brain tissue from the *Synpo* KO mouse by the manufacturer.

Epifluorescence images were acquired with a 2.5× objective on a Zeiss Axio Observer 5 microscope equipped with a Zeiss Axiocam 705 CMOS camera controlled by the ZEN software (version 3.2; RRID:SCR_013672). The Synpo signal was visualized with a filter set for excitation at 450-490 nm and emission at 500-550 nm. The DAPI signal was visualized with a filter set for excitation at 365 nm and emission at 420-470 nm. For both channels, the exposure time was determined by imaging the hippocampus in a Synpo-labeled WT section and applied to all sections from both genotypes.

Histology

The slide-mounted sections were thawed and fixed in 4% formaldehyde as described above. After being washed in purified water, the sections were stained with Cresyl Violet (FD NeuroTechnologies, Columbia, MD; catalog# PS102-01). Following dehydration in ascending grade of ethanol and clearing in xylene, coverslips were applied with DPX mountant. Brightfield images encompassing the hippocampus and the overlaying neocortex were acquired with a 2.5× objective on the same Zeiss Axio Observer 5 microscope using Köhler illumination.

The thickness of layers in the dorsal hippocampal area CA1 was measured from images of parasagittal sections (2 per animal) that best corresponded to 1.4 mm lateral according to a rat brain atlas.[89] FIJI (https://fiji.sc/; RRID:SCR_002285)[90] was used for the measurement along the line that intersects the most dorsal point of the hippocampus and perpendicular to *stratum pyramidale*, from the border between alveus and *stratum oriens* to the hippocampal fissure. Four individual experimenters independently performed measurements masked as to the genotype and the measured thickness was averaged per layer per section.

3DEM

For electron microscopy, the rats (n = 2 per genotype; P80; female) were perfusion-fixed under deep isoflurane anesthesia and tracheal supply of oxygen.[91] The perfusion procedure involved a brief (up to ~20 s) wash with oxygenated Krebs-Ringer Carbicarb buffer (concentration in mM: 2.0 $CaCl_2$, 11.0 D-glucose, 4.7 KCl, 4.0 $MgSO_4$, 118 NaCl, 12.5 Na_2CO_3, 12.5 $NaHCO_3$; pH 7.4; osmolality 300-330 mmol/kg), followed by fixative containing 2.0% formaldehyde, 2.5% glutaraldehyde, 2 mM $CaCl_2$, and 4 mM $MgSO_4$ in 0.1 M

18

cacodylate buffer (pH 7.4) for ~1 hr, during which ~1.9 L of fixative was used per animal (both aldehydes from Ladd Research, Essex Junction, VT). The brains were removed from the skull about 1 hr after the end of perfusion, and stored in the same fixative overnight at RT.

The perfusion-fixed brain tissue was cut into parasagittal sections (250 µm thickness) with a Leica VT1000S vibrating blade microtome. After washes in 0.15 M sodium cacodylate buffer (pH = 7.4), the tissue containing the dorsal hippocampus was stained *en bloc* with reduced osmium (2% osmium tetroxide and 3% potassium ferrocyanide in 0.15 M cacodylate buffer) for 45 min followed by washes in the buffer. The tissue was then treated with 320 mM pyrogallol (aq) for 1 hr. After washes in the buffer, the tissue was stained with 2% osmium tetroxide for 45 min, followed by washes in the buffer and purified water. The tissue was then dehydrated in an ascending series of acetonitrile (25%, 50%, 75%, and twice in 100%). The 50% and 75% acetonitrile solutions also contained 2% uranyl acetate for *en bloc* staining for 20 min each. The tissue was infiltrated and embedded into low-viscosity epoxy resin composed of EMBed-812, nonenyl succinic anhydride, nadic methyl anhydride, and benzyldimethylamine at 60°C for 48-60 hr (all resin components from Electron Microscopy Sciences [EMS], Hatfield, PA).[92] The resin embedded tissue was trimmed to the surface of ~80 µm × 800 µm, exposing the area CA1 of the dorsal hippocampus encompassing the *s. oriens* and *s. radiatum*. Then, 182-302 serial ultrathin sections (nominal thickness of 45 nm) were obtained using a DiATOME 35° diamond knife on a Leica UC7 ultramicrotome. The sections (182-300 per series) were collected usingSynaptek Be-Cu slot grids (EMS or Ted Pella, Redding, CA) that were coated with polyetherimide.

For analysis of the spine apparatus, the serial sections were imaged from the middle of *s. radiatum* (image field centered at ~125 µm from the apical face of *s. pyramidale*), masked as to condition, with a transmission-mode scanning EM (tSEM; Zeiss SUPRA 40 field-emission SEM with a retractable multimode transmitted electron detector and ATLAS package).[93] For the cisternal organelle, the image field centered around the border between *strata oriens* and *pyramidale*. The scan beam at the accelerating voltage of 28 kV was set for a dwell time of 1.3 µs. Each section was imaged from a single field encompassing 49.155 µm × 49.155 µm (24,576 pixels × 24,576 pixels at 2 nm/pixel). The serial tSEM images were aligned using signal whitening Fourier transform (Wetzel et al., 2016) deployed at 3dem.org. EM series with the aligned images were assigned a 5-letter code to mask the identity and genotype of the animal and imported into PyReconstruct (https://github.com/synapseweb/pyreconstruct; RRID:SCR_027562).[94] The pixel size was

19

calibrated using a grating replica (EMS, catalog# 80051), and the average section thickness was calculated with the cylindrical diameter method.[95]

Electrophysiology

Adult male rats (P100-150; n = 7 for WT and n = 8 for KO) were deeply anesthetized with isoflurane and decapitated with guillotine. None of the KO rats used in these experiments showed any signs of renal failure. The brain was removed from the cranium, and the left hippocampus was dissected out and rinsed with room temperature artificial cerebrospinal fluid (aCSF) containing (in mM) 117 NaCl, 5.3 KCl, 26 $NaHCO_3$, 1 NaH2PO$_4$, 2.5 $CaCl_2$, 1.3 $MgSO_4$, and 10 D-glucose, pH 7.4, and bubbled with 95% O_2-5% CO_2. Slices (400 µm thick) from the dorsal hippocampus were cut at 70° transverse to the long axis on a Stoelting tissue chopper and transferred in oxygenated aCSF to the chambers in the Synchroslice system (Lohmann Research Equipment, Castrop-Rauxel, Germany). The dissection and slice preparation took <6 min, which is crucial timing for enduring LTP that lasts >3 hr.[96] Hippocampal slices were placed on a net at the liquid-gas interface between 32-33°C aCSF and humidified 95% O_2-5% CO_2 atmosphere. After 3 h of incubation, the stimulating and recording electrodes were positioned ~400 µm apart in the middle of hippocampal CA1 *s. radiatum* with the stimulating electrode on the CA3 side. Stimuli consisted of 200 µs biphasic current pulses, lasting 100 µs each for positive and negative components of the stimulus. Test pulses (50-250 µA) were given at 1 pulse per 2.5 min unless stated otherwise, and field excitatory postsynaptic potentials (fEPSPs) were recorded. The initial fEPSP slope was ~50% of the maximal fEPSP slope based on the input/output curve for each slice. LTP was induced by three (3T) or eight trains (8T) of TBS with 30 s intervals. Each train of TBS contained 10 bursts at 5 Hz, and each burst contained 4 pulses at 100 Hz.

The delivery of presynaptic stimulation and the acquisition and analysis of fEPSPs were performed with SynchroBrain software (Lohmann Research Equipment). The initial maximum slope was measured over a 0.3-0.5 ms period with position on the waveform held constant in each slice. To calculate the magnitude of LTP, the average of fEPSP slopes during the last 30 min of baseline recordings before the delivery of the TBS was computed and then compared to the average values during the last 20 min of each 1 h or 2 h session following delivery of TBS. Then values across slices (means ± SEM) were presented as times baseline, where 1 indicated no change in the fEPSP slope relative to the pre-TBS baseline.

Blood sample collection

Blood samples (100 µl per animal) were collected from rats (P60-136, n = 16, 4 per genotype per sex) immediately after euthanasia and were centrifuged at 2500 rpm for 15 min. The resulting serum sample was shipped overnight on ice to be analyzed for symmetric dimethylarginine (SDMA) levels by IDEXX (Westbrook, ME).

Anatomical measurements

The body weight was measured three times a week from P25 to P100 (n = 6 each for male WT and KO; n = 6 for female WT and n = 3 for female KO). Because not all animals were weighed on the same days, data was averaged into 4-day bins, with each bin containing measurements for 3 animals. Not all bins contained the same 3 rats. For measuring bone length, the forelimb and hindlimb were removed from euthanized rats (P58-72, n = 12, 3 per sex per genotype). The skin and large muscles were removed with surgical tools, and the remaining soft tissue was dissolved by overnight incubation with agitation at 50°C in a 5% aqueous solution of laundry detergent containing enzymes and oxygen bleach (Pro-Enzyme Laundry Detergent, Absolute Best Cleaning Products LLC, Brookings, SD). The bones were then rinsed in water, and the length was measured from the ulna and tibia using calipers.

Statistics

GraphPad Prism (https://www.graphpad.com/; RRID:SCR_002798) was used for statistical tests described in each figure.

Resource availability

Lead contact

Requests for further information and resources should be directed to and will be fulfilled by the lead contact, Masaaki Kuwajima (masa@mail.clm.utexas.edu).

Materials availability

Rat lines generated in this study have been deposited to the Rat Resource and Research Center (Columbia, MO; https://www.rrrc.us), under the designations LE-Synpo^{em1Kmh} (RRID:RRRC_00964) and LE-Synpo^{em2Kmh} (RRID:RRRC_01025).

Data and code availability

- 3DEM dataset (original EM images and PyReconstruct files) and spreadsheet files containing data on the hippocampal anatomy, SDMA levels, body weight, and bone length have been deposited at the Texas Data Repository (https://doi.org/10.18738/T8/HDOTFV) and 3DEM.org (https://3dem.org/public-data/tapis/public/cloud.data/corral-repl/projects/NeuroNex-3DEM/Public/2025_Kuwajima_Synpo-KO-rats/), and they are publicly available as of the date of publication.

- This paper does not report original code.

- Any additional information required to reanalyze the data reported in this paper is available from the lead contact upon request.

Acknowledgments

Author Contributions

Conceptualization: MK, LMK, KMH

Funding acquisition: KMH

Methodology: MK, OIO, LMK, SS, KMH

Investigation: MK, OIO, AA, WY, SS, AX, AL, EP

Data curation: MK, OIO, WY, KMH

Formal analysis: MK, OIO, AA, WY, SS, AX, AL, EP, KMH

Visualization: MK, OIO, LMK, AA, WY, SS, AX, AL, EP

Writing – original draft: MK, OIO, SS

Writing – review and editing: MK, OIO, LMK, WY, KMH

Supervision and Project administration: MK, KMH

Declaration of Interests

The authors declare no competing interests.

Declaration of Generative AI and AI-assisted Technologies

The authors did not use generative AI and AI-assisted technologies during the preparation of this work.

Supplemental information

Document S1.

Additional Resources

The Harris lab wiki describing details of 3DEM procedures (perfusion-fixation, tissue processing, and imaging): https://cloud.wikis.utexas.edu/wiki/spaces/khlab/

References

1. Deller, T., Korte, M., Chabanis, S., Drakew, A., Schwegler, H., Stefani, G.G., Zuniga, A., Schwarz, K., Bonhoeffer, T., Zeller, R., et al. (2003). Synaptopodin-deficient mice lack a spine apparatus and show deficits in synaptic plasticity. Proc. Natl. Acad. Sci. U. S. A. *100*, 10494–10499. https://doi.org/10.1073/pnas.1832384100.

2. Bas Orth, C., Schultz, C., Müller, C.M., Frotscher, M., and Deller, T. (2007). Loss of the cisternal organelle in the axon initial segment of cortical neurons in synaptopodin-deficient mice. J. Comp. Neurol. *504*, 441–449. https://doi.org/10.1002/cne.21445.

3. Falahati, H., Wu, Y., Fang, M., and De Camilli, P. (2024). Ectopic reconstitution of a spine-apparatus-like structure provides insight into mechanisms underlying its formation. Curr. Biol. https://doi.org/10.1016/j.cub.2024.11.010.

4. Korkotian, E., and Segal, M. (2011). Synaptopodin regulates release of calcium from stores in dendritic spines of cultured hippocampal neurons. J. Physiol. *589*, 5987–5995. https://doi.org/10.1113/jphysiol.2011.217315.

5. Asanuma, K., Kim, K., Oh, J., Giardino, L., Chabanis, S., Faul, C., Reiser, J., and Mundel, P. (2005). Synaptopodin regulates the actin-bundling activity of α-actinin in an isoform-specific manner. J. Clin. Invest. *115*, 1188–1198. https://doi.org/doi:10.1172/JCI23371.

6. Kwon, S.K., Kim, S.J., and Kim, H.-Y. (2016). Urine synaptopodin excretion is an important marker of glomerular disease progression. Korean J. Intern. Med. *31*, 938–943. https://doi.org/10.3904/kjim.2015.226.

7. Hirakawa, M., Tsuruya, K., Yotsueda, H., Tokumoto, M., Ikeda, H., Katafuchi, R., Fujimi, S., Hirakata, H., and Iida, M. (2006). Expression of synaptopodin and GLEPP1 as markers of steroid responsiveness in primary focal segmental glomerulosclerosis. Life Sci. *79*, 757–763. https://doi.org/10.1016/j.lfs.2006.02.031.

8. Datta, A., Chai, Y.L., Tan, J.M., Lee, J.H., Francis, P.T., Chen, C.P., Sze, S.K., and Lai, M.K.P. (2017). An iTRAQ-based proteomic analysis reveals dysregulation of neocortical synaptopodin in Lewy body dementias. Mol. Brain *10*, 36. https://doi.org/10.1186/s13041-017-0316-9.

9. Goetzl, L., Merabova, N., Darbinian, N., Martirosyan, D., Poletto, E., Fugarolas, K., and Menkiti, O. (2017). Diagnostic Potential of Neural Exosome Cargo as Biomarkers for Acute Brain Injury. Ann. Clin. Transl. Neurol. *5*, 4–10. https://doi.org/10.1002/acn3.499.

10. Sánchez-Ponce, D., Blázquez-Llorca, L., DeFelipe, J., Garrido, J.J., and Muñoz, A. (2012). Colocalization of α-actinin and Synaptopodin in the Pyramidal Cell Axon Initial Segment. Cereb. Cortex *22*, 1648–1661. https://doi.org/10.1093/cercor/bhr251.

11. Jungenitz, T., Bird, A., Engelhardt, M., Jedlicka, P., Schwarzacher, S.W., and Deller, T. (2023). Structural plasticity of the axon initial segment in rat hippocampal granule cells following high frequency stimulation and LTP induction. Front. Neuroanat. *17*. https://doi.org/10.3389/fnana.2023.1125623.

12. Vlachos, A., Maggio, N., and Segal, M. (2008). Lack of correlation between synaptopodin expression and the ability to induce LTP in the rat dorsal and ventral hippocampus. Hippocampus *18*, 1–4. https://doi.org/10.1002/hipo.20373.

13. Holbro, N., Grunditz, Å., and Oertner, T.G. (2009). Differential distribution of endoplasmic reticulum controls metabotropic signaling and plasticity at hippocampal synapses. Proc. Natl. Acad. Sci. *106*, 15055–15060. https://doi.org/10.1073/pnas.0905110106.

14. Špaček, J. (1985). Three-dimensional analysis of dendritic spines. II. Spine apparatus and other cytoplasmic components. Anat. Embryol. (Berl.) *171*, 235–243. https://doi.org/10.1007/BF00341418.

15. Pierce, J.P., Mayer, T., and McCarthy, J.B. (2001). Evidence for a satellite secretory pathway in neuronal dendritic spines. Curr. Biol. *11*, 351–355. https://doi.org/10.1016/S0960-9822(01)00077-X.

16. Pierce, J.P., van Leyen, K., and McCarthy, J.B. (2000). Translocation machinery for synthesis of integral membrane and secretory proteins in dendritic spines. Nat Neurosci *3*, 311–313. https://doi.org/10.1038/73868.

17. Kruse, P., Brandes, G., Hemeling, H., Huang, Z., Wrede, C., Hegermann, J., Vlachos, A., and Lenz, M. (2024). Synaptopodin Regulates Denervation-Induced Plasticity at Hippocampal Mossy Fiber Synapses. Cells *13*, 114. https://doi.org/10.3390/cells13020114.

18. Yamazaki, M., Matsuo, R., Fukazawa, Y., Ozawa, F., and Inokuchi, K. (2001). Regulated expression of an actin-associated protein, synaptopodin, during long-term potentiation. J. Neurochem. *79*, 192–199. https://doi.org/10.1046/j.1471-4159.2001.00552.x.

19. Fukazawa, Y., Saitoh, Y., Ozawa, F., Ohta, Y., Mizuno, K., and Inokuchi, K. (2003). Hippocampal LTP Is Accompanied by Enhanced F-Actin Content within the Dendritic Spine that Is Essential for Late LTP Maintenance In Vivo. Neuron *38*, 447–460. https://doi.org/10.1016/S0896-6273(03)00206-X.

20. Korkotian, E., Frotscher, M., and Segal, M. (2014). Synaptopodin Regulates Spine Plasticity: Mediation by Calcium Stores. J. Neurosci. *34*, 11641–11651. https://doi.org/10.1523/JNEUROSCI.0381-14.2014.

21. Vlachos, A., Korkotian, E., Schonfeld, E., Copanaki, E., Deller, T., and Segal, M. (2009). Synaptopodin Regulates Plasticity of Dendritic Spines in Hippocampal Neurons. J Neurosci *29*, 1017–1033. https://doi.org/10.1523/JNEUROSCI.5528-08.2009.

22. Chirillo, M.A., Waters, M.S., Lindsey, L.F., Bourne, J.N., and Harris, K.M. (2019). Local resources of polyribosomes and SER promote synapse enlargement and spine clustering after long-term potentiation in adult rat hippocampus. Sci. Rep. *9*, 3861. https://doi.org/10.1038/s41598-019-40520-x.

23. Benedeczky, I., Molnár, E., and Somogyi, P. (1994). The cisternal organelle as a Ca2+-storing compartment associated with GABAergic synapses in the axon initial segment of hippocampal pyramidal neurones. Exp. Brain Res. *101*, 216–230. https://doi.org/10.1007/BF00228742.

24. King, A.N., Manning, C.F., and Trimmer, J.S. (2014). A unique ion channel clustering domain on the axon initial segment of mammalian neurons. J. Comp. Neurol. *522*, 2594–2608. https://doi.org/10.1002/cne.23551.

25. Lipkin, A.M., Cunniff, M.M., Spratt, P.W.E., Lemke, S.M., and Bender, K.J. (2021). Functional Microstructure of CaV-Mediated Calcium Signaling in the Axon Initial Segment. J. Neurosci. *41*, 3764–3776. https://doi.org/10.1523/JNEUROSCI.2843-20.2021.

26. Schlüter, A., Del Turco, D., Deller, T., Gutzmann, A., Schultz, C., and Engelhardt, M. (2017). Structural Plasticity of Synaptopodin in the Axon Initial Segment during Visual Cortex Development. Cereb. Cortex *27*, 4662–4675. https://doi.org/10.1093/cercor/bhx208.

27. Asanuma, K., Yanagida-Asanuma, E., Faul, C., Tomino, Y., Kim, K., and Mundel, P. (2006). Synaptopodin orchestrates actin organization and cell motility via regulation of RhoA signalling. Nat Cell Biol *8*, 485–491. https://doi.org/10.1038/ncb1400.

28. Faul, C., Donnelly, M., Merscher-Gomez, S., Chang, Y.H., Franz, S., Delfgaauw, J., Chang, J.-M., Choi, H.Y., Campbell, K.N., Kim, K., et al. (2008). The actin cytoskeleton of kidney podocytes is a direct target of the antiproteinuric effect of cyclosporine A. Nat. Med. *14*, 931–938. https://doi.org/10.1038/nm.1857.
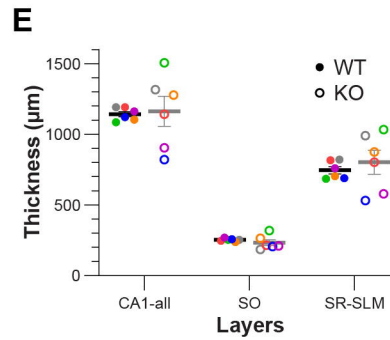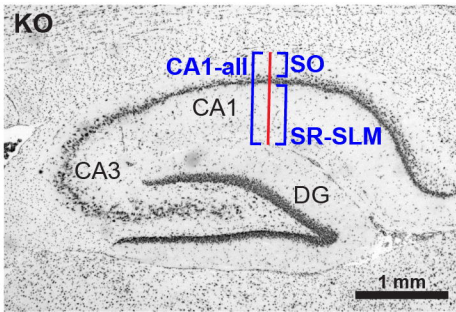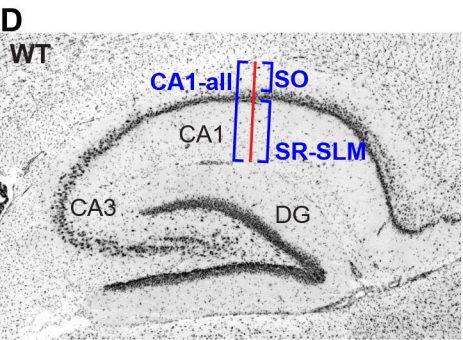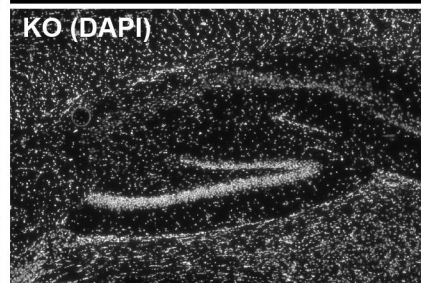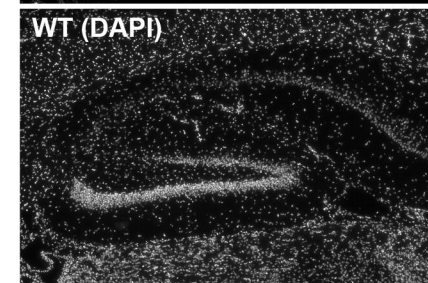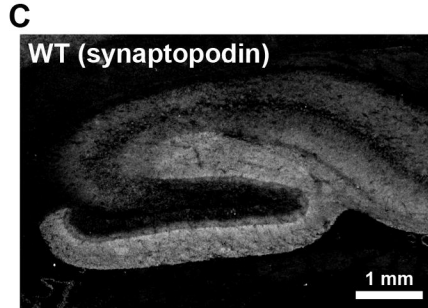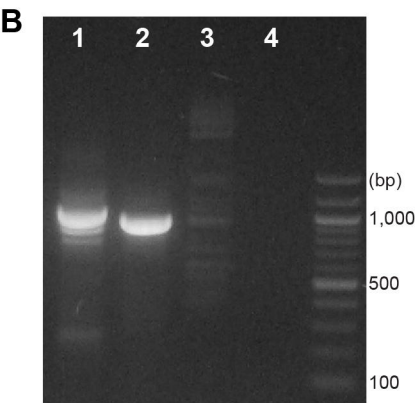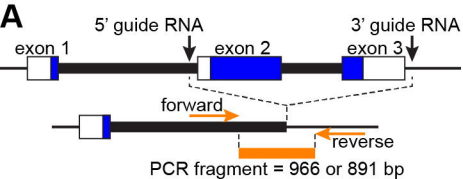
29. Buvall, L., Wallentin, H., Sieber, J., Andreeva, S., Choi, H.Y., Mundel, P., and Greka, A. (2017). Synaptopodin Is a Coincidence Detector of Tyrosine versus Serine/Threonine Phosphorylation for the Modulation of Rho Protein Crosstalk in Podocytes. J. Am. Soc. Nephrol. *28*, 837–851. https://doi.org/10.1681/ASN.2016040414.

30. Ning, L., Suleiman, H.Y., and Miner, J.H. (2020). Synaptopodin Is Dispensable for Normal Podocyte Homeostasis but Is Protective in the Context of Acute Podocyte Injury. J. Am. Soc. Nephrol. *31*, 2815–2832. https://doi.org/10.1681/ASN.2020050572.

31. Jedlicka, P., Schwarzacher, S.W., Winkels, R., Kienzler, F., Frotscher, M., Bramham, C.R., Schultz, C., Bas Orth, C., and Deller, T. (2009). Impairment of in vivo theta-burst long-term potentiation and network excitability in the dentate gyrus of synaptopodin-deficient mice lacking the spine apparatus and the cisternal organelle. Hippocampus *19*, 130–140. https://doi.org/10.1002/hipo.20489.

32. Zhang, X., Pöschel, B., Faul, C., Upreti, C., Stanton, P.K., and Mundel, P. (2013). Essential Role for Synaptopodin in Dendritic Spine Plasticity of the Developing Hippocampus. J. Neurosci. *33*, 12510–12518. https://doi.org/10.1523/JNEUROSCI.2983-12.2013.

33. Grigoryan, G., and Segal, M. (2016). Ryanodine-mediated conversion of STP to LTP is lacking in synaptopodin-deficient mice. Brain Struct. Funct. *221*, 2393–2397. https://doi.org/10.1007/s00429-015-1026-7.

34. Wu, P.Y., Inglebert, Y., and McKinney, R.A. (2024). Synaptopodin: a key regulator of Hebbian plasticity. Front. Cell. Neurosci. *18*. https://doi.org/10.3389/fncel.2024.1482844.

35. Inglebert, Y., Wu, P.Y., Tourbina-Kolomiets, J., Dang, C.L., and McKinney, R.A. (2024). Synaptopodin is required for long-term depression at Schaffer collateral-CA1 synapses. Mol. Brain *17*, 17. https://doi.org/10.1186/s13041-024-01089-3.

36. Ostrovskaya, O.I., Cao, G., Eroglu, C., and Harris, K.M. (2020). Developmental onset of enduring long-term potentiation in mouse hippocampus. Hippocampus *30*, 1298–1312. https://doi.org/10.1002/hipo.23257.

37. Kirov, S.A., Goddard, C.A., and Harris, K.M. (2004). Age-dependence in the homeostatic upregulation of hippocampal dendritic spine number during blocked synaptic transmission. Neuropharmacology *47*, 640–648. https://doi.org/10.1016/j.neuropharm.2004.07.039.

38. Cao, G., and Harris, K.M. (2012). Developmental regulation of the late phase of long-term potentiation (L-LTP) and metaplasticity in hippocampal area CA1 of the rat. J. Neurophysiol. *107*, 902–912. https://doi.org/10.1152/jn.00780.2011.

39. Watson, D.J., Ostroff, L., Cao, G., Parker, P.H., Smith, H., and Harris, K.M. (2016). LTP enhances synaptogenesis in the developing hippocampus. Hippocampus *26*, 560–576. https://doi.org/10.1002/hipo.22536.

40. Harris, K.M. (2020). Structural LTP: from synaptogenesis to regulated synapse enlargement and clustering. Curr. Opin. Neurobiol. *63*, 189–197. https://doi.org/10.1016/j.conb.2020.04.009.

41. Mundel, P., Heid, H.W., Mundel, T.M., Kruger, M., Reiser, J., and Kriz, W. (1997). Synaptopodin: An Actin-associated Protein in Telencephalic Dendrites and Renal Podocytes. J Cell Biol *139*, 193–204. https://doi.org/10.1083/jcb.139.1.193.

42. Czarnecki, K., Haas, C.A., Bas Orth, C., Deller, T., and Frotscher, M. (2005). Postnatal development of synaptopodin expression in the rodent hippocampus. J. Comp. Neurol. *490*, 133–144. https://doi.org/10.1002/cne.20651.
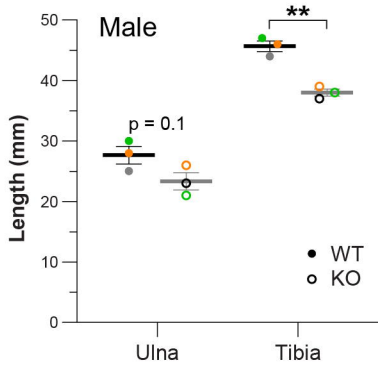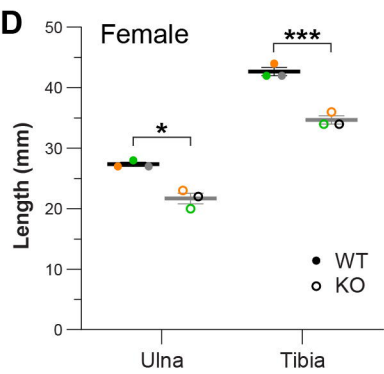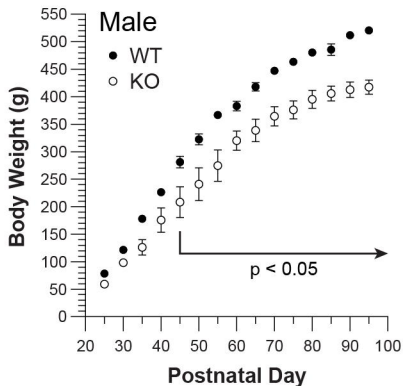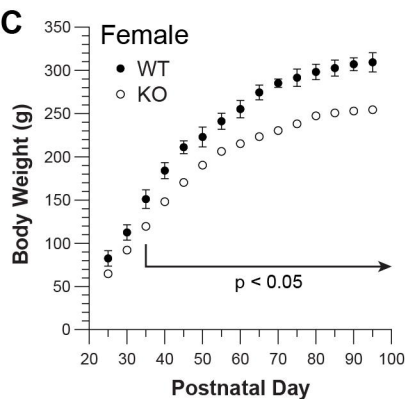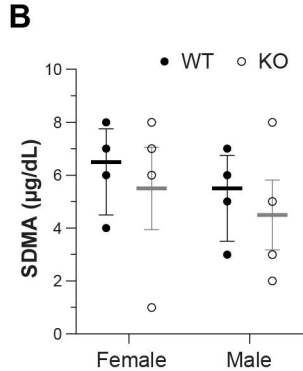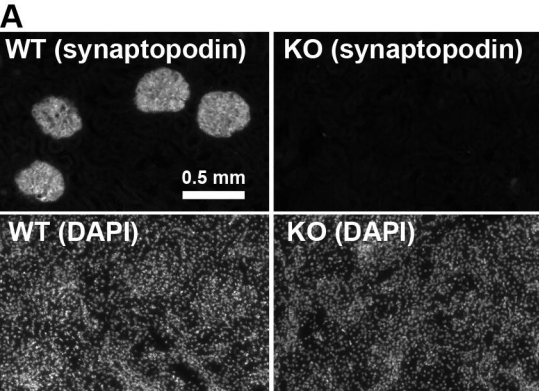
43. Špaček, J., and Harris, K.M. (1997). Three-Dimensional Organization of Smooth Endoplasmic Reticulum in Hippocampal CA1 Dendrites and Dendritic Spines of the Immature and Mature Rat. J Neurosci *17*, 190–203.

44. Cooney, J.R., Hurlburt, J.L., Selig, D.K., Harris, K.M., and Fiala, J.C. (2002). Endosomal Compartments Serve Multiple Hippocampal Dendritic Spines from a Widespread Rather Than a Local Store of Recycling Membrane. J Neurosci *22*, 2215–2224.

45. Al Banchaabouchi, M., Marescau, B., Possemiers, I., D'Hooge, R., Levillain, O., and De Deyn, P.P. (2000). NG,NG-Dimethylarginine and NG,N'G-dimethylarginine in renal insufficiency. Pflüg. Arch. *439*, 524–531. https://doi.org/10.1007/s004249900220.

46. Coyne, M.J., Schultze, A.E., Iii, D.J.M., Murphy, R.E., Cross, J., Strong-Townsend, M., Drake, C., and Mack, R. (2022). Evaluation of renal injury and function biomarkers, including symmetric dimethylarginine (SDMA), in the rat passive Heymann nephritis (PHN) model. PLOS ONE *17*, e0269085. https://doi.org/10.1371/journal.pone.0269085.

47. Hamlin, D.M., Schultze, A.E., Coyne, M.J., McCrann, D.J.I., Mack, R., Drake, C., Murphy, R.E., Cross, J., Strong-Townsend, M., Yerramilli, M., et al. (2022). Evaluation of Renal Biomarkers, Including Symmetric Dimethylarginine, following Gentamicin-Induced Proximal Tubular Injury in the Rat. Kidney360 *3*, 341. https://doi.org/10.34067/KID.0006542020.

48. Kohnken, R., Himmel, L., Logan, M., Peterson, R., Biswas, S., Dunn, C., and LeRoy, B. (2022). Symmetric Dimethylarginine Is a Sensitive Biomarker of Glomerular Injury in Rats. Toxicol. Pathol. *50*, 176–185. https://doi.org/10.1177/01926233211045341.

49. Fiala, J.C., and Harris, K.M. (2001). Extending Unbiased Stereology of Brain Ultrastructure to Three-dimensional Volumes. J. Am. Med. Inform. Assoc. *8*, 1–16. https://doi.org/10.1136/jamia.2001.0080001.

50. Palay, S.L., Sotelo, C., Peters, A., and Orkand, P.M. (1968). THE AXON HILLOCK AND THE INITIAL SEGMENT. J Cell Biol *38*, 193–201. https://doi.org/10.1083/jcb.38.1.193.

51. Peters, A., Proskauer, C.C., and Kaiserman-Abramof, I.R. (1968). THE SMALL PYRAMIDAL NEURON OF THE RAT CEREBRAL CORTEX: The Axon Hillock and Initial Segment. J Cell Biol *39*, 604–619. https://doi.org/10.1083/jcb.39.3.604.

52. Moor, M.B., and Bonny, O. (2016). Ways of calcium reabsorption in the kidney. Am. J. Physiol.-Ren. Physiol. *310*, F1337–F1350. https://doi.org/10.1152/ajprenal.00273.2015.

53. Staruschenko, A., Alexander, R.T., Caplan, M.J., and Ilatovskaya, D.V. (2024). Calcium signalling and transport in the kidney. Nat. Rev. Nephrol. *20*, 541–555. https://doi.org/10.1038/s41581-024-00835-z.

54. Yu, Y., Fuscoe, J.C., Zhao, C., Guo, C., Jia, M., Qing, T., Bannon, D.I., Lancashire, L., Bao, W., Du, T., et al. (2014). A rat RNA-Seq transcriptomic BodyMap across 11 organs and 4 developmental stages. Nat. Commun. *5*, 3230. https://doi.org/10.1038/ncomms4230.

55. Yue, F., Cheng, Y., Breschi, A., Vierstra, J., Wu, W., Ryba, T., Sandstrom, R., Ma, Z., Davis, C., Pope, B.D., et al. (2014). A comparative encyclopedia of DNA elements in the mouse genome. Nature *515*, 355–364. https://doi.org/10.1038/nature13992.

56. Schultz, R.L., and Karlsson, U. (1966). Spine apparatus occurrence during different fixation procedures. J. Ultrastruct. Res. *14*, 268–276. https://doi.org/10.1016/S0022-5320(66)80048-5.

57. Westrum, L.E., Jones, D.H., Gray, E.G., and Barron, J. (1980). Microtubules, dendritic spines and spine apparatuses. Cell Tissue Res. *208*, 171–181. https://doi.org/10.1007/BF00234868.
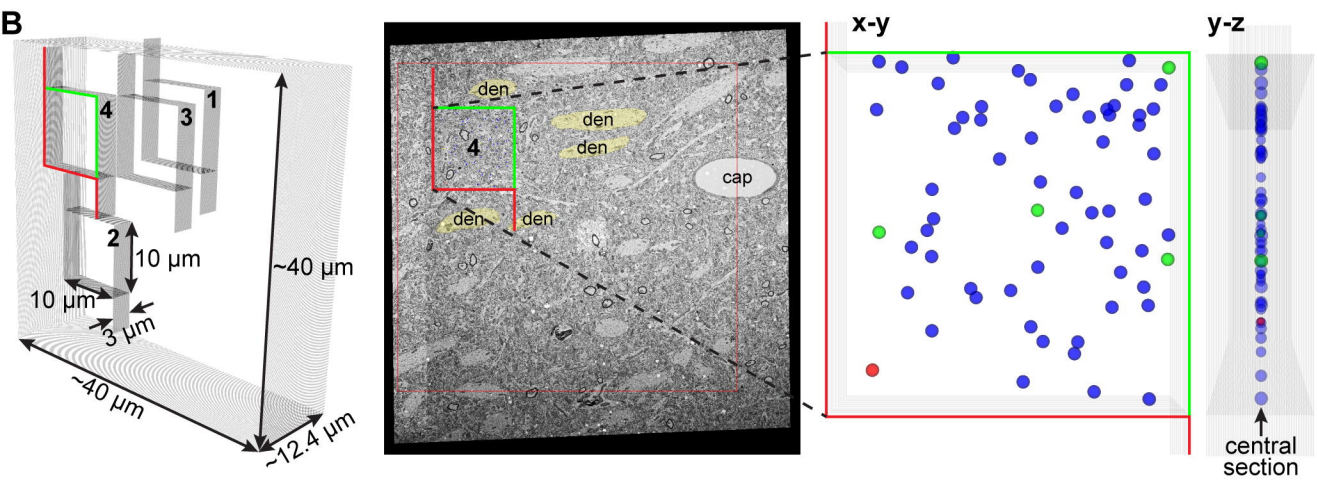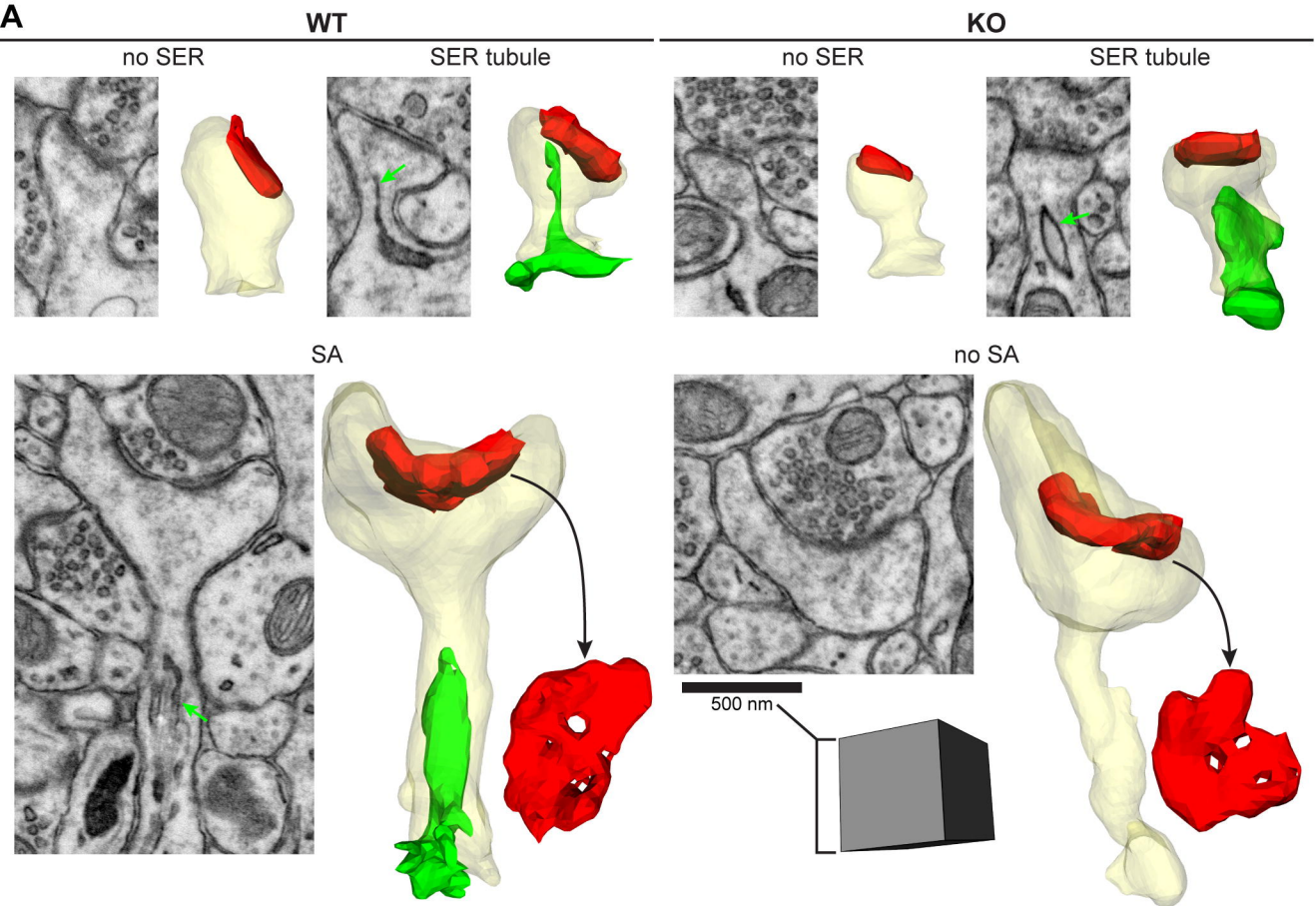
58. Terasaki, M., and Reese, T.S. (1992). Characterization of endoplasmic reticulum by co-localization of BiP and dicarbocyanine dyes. J. Cell Sci. *101*, 315–322. https://doi.org/10.1242/jcs.101.2.315.

59. Martone, M., Zhang, Y., Simpliciano, V., Carragher, B., and Ellisman, M. (1993). Three-dimensional visualization of the smooth endoplasmic reticulum in Purkinje cell dendrites. J Neurosci *13*, 4636–4646.

60. Ehlers, M.D. (2013). Dendritic trafficking for neuronal growth and plasticity. Biochem. Soc. Trans. *41*, 1365–1382. https://doi.org/10.1042/BST20130081.

61. Martínez, G., Khatiwada, S., Costa-Mattioli, M., and Hetz, C. (2018). ER Proteostasis Control of Neuronal Physiology and Synaptic Function. Trends Neurosci. *41*, 610–624. https://doi.org/10.1016/j.tins.2018.05.009.

62. Perez-Alvarez, A., Yin, S., Schulze, C., Hammer, J.A., Wagner, W., and Oertner, T.G. (2020). Endoplasmic reticulum visits highly active spines and prevents runaway potentiation of synapses. Nat. Commun. *11*, 5083. https://doi.org/10.1038/s41467-020-18889-5.

63. Deller, T., Bas Orth, C., Del Turco, D., Vlachos, A., Burbach, G.J., Drakew, A., Chabanis, S., Korte, M., Schwegler, H., Haas, C.A., et al. (2007). A role for synaptopodin and the spine apparatus in hippocampal synaptic plasticity. Ann. Anat. - Anat. Anz. *189*, 5–16. https://doi.org/10.1016/j.aanat.2006.06.013.

64. Cui-Wang, T., Hanus, C., Cui, T., Helton, T., Bourne, J., Watson, D., Harris, K.M., and Ehlers, M.D. (2012). Local Zones of Endoplasmic Reticulum Complexity Confine Cargo in Neuronal Dendrites. Cell *148*, 309–321. https://doi.org/10.1016/j.cell.2011.11.056.

65. Gilbert, E.T., Klaver, L.M.F., Arndt, K.C., Kim, J., Jia, X., McKenzie, S., and English, D.F. (2025). Reciprocal interactions between CA1 pyramidal and axo-axonic cells control sharp wave-ripple events. Preprint at bioRxiv, https://doi.org/10.1101/2024.07.02.601726 https://doi.org/10.1101/2024.07.02.601726.

66. Gallo, N.B., Paul, A., and Aelst, L.V. (2020). Shedding Light on Chandelier Cell Development, Connectivity, and Contribution to Neural Disorders. Trends Neurosci. *43*, 565–580. https://doi.org/10.1016/j.tins.2020.05.003.

67. Schneider-Mizell, C.M., Bodor, A.L., Collman, F., Brittain, D., Bleckert, A., Dorkenwald, S., Turner, N.L., Macrina, T., Lee, K., Lu, R., et al. (2021). Structure and function of axo-axonic inhibition. eLife *10*, e73783. https://doi.org/10.7554/eLife.73783.

68. Dudok, B., Szoboszlay, M., Paul, A., Klein, P.M., Liao, Z., Hwaun, E., Szabo, G.G., Geiller, T., Vancura, B., Wang, B.-S., et al. (2021). Recruitment and inhibitory action of hippocampal axo-axonic cells during behavior. Neuron *109*, 3838-3850.e8. https://doi.org/10.1016/j.neuron.2021.09.033.

69. Aika, Y., Ren, J.Q., Kosaka, K., and Kosaka, T. (1994). Quantitative analysis of GABA-like-immunoreactive and parvalbumin-containing neurons in the CA1 region of the rat hippocampus using a stereological method, the disector. Exp. Brain Res. *99*, 267–276. https://doi.org/10.1007/BF00239593.

70. Jinno, S., and Kosaka, T. (2010). Stereological estimation of numerical densities of glutamatergic principal neurons in the mouse hippocampus. Hippocampus *20*, 829–840. https://doi.org/10.1002/hipo.20685.

71. Routh, B.N., Johnston, D., Harris, K., and Chitwood, R.A. (2009). Anatomical and Electrophysiological Comparison of CA1 Pyramidal Neurons of the Rat and Mouse. J. Neurophysiol. *102*, 2288–2302. https://doi.org/10.1152/jn.00082.2009.

72. Vitale, P., Librizzi, F., Vaiana, A.C., Capuana, E., Pezzoli, M., Shi, Y., Romani, A., Migliore, M., and Migliore, R. (2023). Different responses of mice and rats hippocampus CA1 pyramidal neurons to in vitro and in vivo-like inputs. Front. Cell. Neurosci. *17*. https://doi.org/10.3389/fncel.2023.1281932.
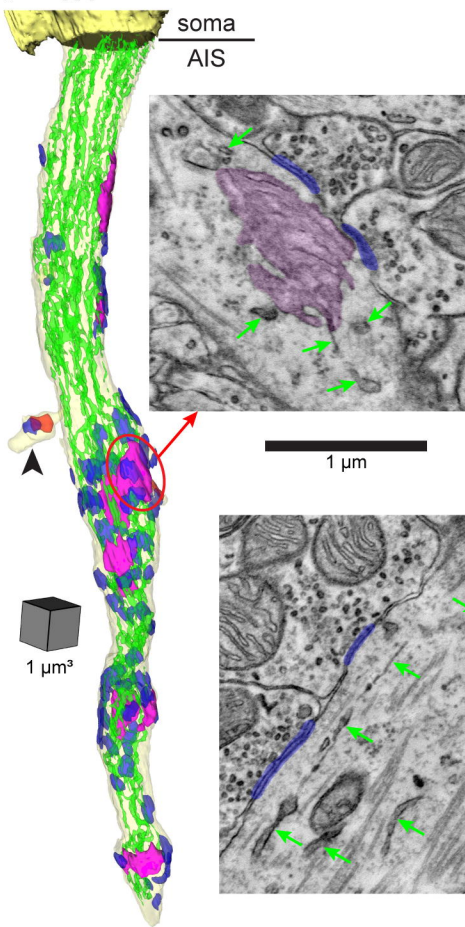
73. Bourne, J.N., and Harris, K.M. (2011). Coordination of size and number of excitatory and inhibitory synapses results in a balanced structural plasticity along mature hippocampal CA1 dendrites during LTP. Hippocampus *21*, 354–373. https://doi.org/10.1002/hipo.20768.

74. Raymond, C.R. (2007). LTP forms 1, 2 and 3: different mechanisms for the 'long' in long-term potentiation. Trends Neurosci. *30*, 167–175. https://doi.org/10.1016/j.tins.2007.01.007.

75. Reddy, P.H., Mani, G., Park, B.S., Jacques, J., Murdoch, G., Whetsell Jr., W., Kaye, J., and Manczak, M. (2005). Differential loss of synaptic proteins in Alzheimer's disease: Implications for synaptic dysfunction. J. Alzheimers Dis. *7*, 103–117.

76. Vasil'ev, D.S., Tumanova, N.L., and Zhuravin, I.A. (2010). [Study of distribution of protein of the spine apparatus synaptopodin in cortical brain parts of rats submitted to hypoxia at different periods of embryogenesis]. Zhurnal Evoliutsionnoĭ Biokhimii Fiziol. *46*, 435–439.

77. Cohen, J.W., Louneva, N., Han, L., Hodes, G.E., Wilson, R.S., Bennett, D.A., Lucki, I., and Arnold, S.E. (2011). Chronic corticosterone exposure alters postsynaptic protein levels of PSD-95, NR1, and synaptopodin in the mouse brain. Synapse *65*, 763–770. https://doi.org/10.1002/syn.20900.

78. Arnold, S.E., Louneva, N., Cao, K., Wang, L.-S., Han, L.-Y., Wolk, D.A., Negash, S., Leurgans, S.E., Schneider, J.A., Buchman, A.S., et al. (2013). Cellular, synaptic, and biochemical features of resilient cognition in Alzheimer's disease. Neurobiol. Aging *34*, 157–168. https://doi.org/10.1016/j.neurobiolaging.2012.03.004.

79. Strehl, A., Lenz, M., Itsekson-Hayosh, Z., Becker, D., Chapman, J., Deller, T., Maggio, N., and Vlachos, A. (2014). Systemic inflammation is associated with a reduction in Synaptopodin expression in the mouse hippocampus. Exp. Neurol. *261*, 230–235. https://doi.org/10.1016/j.expneurol.2014.04.033.

80. Goetzl, E.J., Kapogiannis, D., Schwartz, J.B., Lobach, I.V., Goetzl, L., Abner, E.L., Jicha, G.A., Karydas, A.M., Boxer, A., and Miller, B.L. (2016). Decreased synaptic proteins in neuronal exosomes of frontotemporal dementia and Alzheimer's disease. FASEB J. *30*, 4141–4148. https://doi.org/10.1096/fj.201600816R.

81. Bhargava, P., Nogueras-Ortiz, C., Kim, S., Delgado-Peraza, F., Calabresi, P.A., and Kapogiannis, D. (2021). Synaptic and complement markers in extracellular vesicles in multiple sclerosis. Mult. Scler. J. *27*, 509–518. https://doi.org/10.1177/1352458520924590.

82. Sauer, B., and Henderson, N. (1988). Site-specific DNA recombination in mammalian cells by the Cre recombinase of bacteriophage P1. Proc. Natl. Acad. Sci. *85*, 5166–5170. https://doi.org/10.1073/pnas.85.14.5166.

83. Schönig, K., Weber, T., Frömmig, A., Wendler, L., Pesold, B., Djandji, D., Bujard, H., and Bartsch, D. (2012). Conditional gene expression systems in the transgenic rat brain. BMC Biol. *10*, 77. https://doi.org/10.1186/1741-7007-10-77.

84. Fornasiero, E.F., Mandad, S., Wildhagen, H., Alevra, M., Rammner, B., Keihani, S., Opazo, F., Urban, I., Ischebeck, T., Sakib, M.S., et al. (2018). Precisely measured protein lifetimes in the mouse brain reveal differences across tissues and subcellular fractions. Nat. Commun. *9*, 4230. https://doi.org/10.1038/s41467-018-06519-0.

85. Concordet, J.-P., and Haeussler, M. (2018). CRISPOR: intuitive guide selection for CRISPR/Cas9 genome editing experiments and screens. Nucleic Acids Res. *46*, W242–W245. https://doi.org/10.1093/nar/gky354.

86. Marcondes, F.K., Bianchi, F.J., and Tanno, A.P. (2002). Determination of the estrous cycle phases of rats: some helpful considerations. Braz. J. Biol. *62*, 609–614. https://doi.org/10.1590/S1519-69842002000400008.

87. Byers, S.L., Wiles, M.V., Dunn, S.L., and Taft, R.A. (2012). Mouse Estrous Cycle Identification Tool and Images. PLOS ONE *7*, e35538. https://doi.org/10.1371/journal.pone.0035538.

88. Becker, J.B., Arnold, A.P., Berkley, K.J., Blaustein, J.D., Eckel, L.A., Hampson, E., Herman, J.P., Marts, S., Sadee, W., Steiner, M., et al. (2005). Strategies and Methods for Research on Sex Differences in Brain and Behavior. Endocrinology *146*, 1650–1673. https://doi.org/10.1210/en.2004-1142.

89. Paxinos, G., and Watson, C. (2007). The rat brain in stereotaxic coordinates 6th Edition. (Academic Press).

90. Schindelin, J., Arganda-Carreras, I., Frise, E., Kaynig, V., Longair, M., Pietzsch, T., Preibisch, S., Rueden, C., Saalfeld, S., Schmid, B., et al. (2012). Fiji: an open-source platform for biological-image analysis. Nat. Methods *9*, 676–682. https://doi.org/10.1038/nmeth.2019.

91. Kuwajima, M., Mendenhall, J.M., and Harris, K.M. (2013). Large-Volume Reconstruction of Brain Tissue from High-Resolution Serial Section Images Acquired by SEM-Based Scanning Transmission Electron Microscopy. Methods Mol. Biol. Clifton NJ *950*, 253–273. https://doi.org/10.1007/978-1-62703-137-0_15.

92. Mascorro, J.A. (2009). Novel choices for formulating embedding media kits. In Scanning Microscopy 2009 (International Society for Optics and Photonics), p. 73780F. https://doi.org/10.1117/12.821821.

93. Kuwajima, M., Mendenhall, J.M., Lindsey, L.F., and Harris, K.M. (2013). Automated Transmission-Mode Scanning Electron Microscopy (tSEM) for Large Volume Analysis at Nanoscale Resolution. PLoS ONE *8*, e59573. https://doi.org/10.1371/journal.pone.0059573.

94. Chirillo, M.A., Falco, J.N., Musslewhite, M.D., Lindsey, L.F., and Harris, K.M. (2025). PyReconstruct: A fully open-source, collaborative successor to Reconstruct. Proc. Natl. Acad. Sci. *122*, e2505822122. https://doi.org/10.1073/pnas.2505822122.

95. Fiala, J.C., and Harris, K.M. (2001). Cylindrical diameters method for calibrating section thickness in serial electron microscopy. J. Microsc. *202*, 468–472. https://doi.org/10.1046/j.1365-2818.2001.00926.x.

96. Reymann, K.G., and Frey, J.U. (2007). The late maintenance of hippocampal LTP: Requirements, phases, 'synaptic tagging', 'late-associativity' and implications. Neuropharmacology *52*, 24–40. https://doi.org/10.1016/j.neuropharm.2006.07.026.

A 5' guide RNA — 3' guide RNA; exon 1, exon 2, exon 3; forward, reverse; PCR fragment = 966 or 891 bp

B Gel lanes 1, 2, 3, 4; (bp) markers 1,000, 500, 100

C WT (synaptopodin), KO (synaptopodin), WT (DAPI), KO (DAPI); scale bar 1 mm

D WT and KO; CA1-all, SO, CA1, SR-SLM, CA3, DG; scale bar 1 mm

E Thickness (μm) vs Layers (CA1-all, SO, SR-SLM); WT (filled), KO (open)

A

WT (synaptopodin)   KO (synaptopodin)

0.5 mm

WT (DAPI)   KO (DAPI)

B

● WT   ○ KO

SDMA (μg/dL)

10
8
6
4
2
0

Female   Male

C

Female

Body Weight (g)

350
300
250
200
150
100
50
0

● WT
○ KO

p < 0.05

20 30 40 50 60 70 80 90 100

Postnatal Day

Male

Body Weight (g)

550
500
450
400
350
300
250
200
150
100
50
0

● WT
○ KO

p < 0.05

20 30 40 50 60 70 80 90 100

Postnatal Day

D

Female

Length (mm)

50
40
30
20
10
0

*

***

Ulna   Tibia

● WT
○ KO

Male

Length (mm)

50
40
30
20
10
0

p = 0.1

**

Ulna   Tibia

● WT
○ KO

A

WT

no SER SER tubule

KO

no SER SER tubule

SA

no SA

500 nm

B

den
den
den
cap
den den

4
1
3
2

10 µm
10 µm
3 µm
~40 µm
~40 µm
~12.4 µm

x-y

y-z

central
section

A WT

soma
AIS

1 μm

1 μm³

B KO

soma
AIS

1 μm³

1 μm³

myelin AIS